GEOCHEMISTRY

Ventilation of the deep Gulf of Mexico and potential insights to the Atlantic Meridional Overturning Circulation

Rainer M.W. Amon[1,2]*, Jose Ochoa[3]†, Julio Candela[3]†, Sharon Z. Herzka[3], Paula Pérez-Brunius[3], Julio Sheinbaum[3], Víctor F. Camacho Ibar[4], Juan Carlos Herguera[3], Martin Hernández Ayon[4], Robert M. Key[5], Sergey Molodtsov[2]‡

Ventilation in the deep Gulf of Mexico (GoM), its connection to the North Atlantic, and its susceptibility to changes of the Atlantic Meridional Overturning Circulation are investigated by combining observations of radiocarbon and volume transport with a Coupled Model Intercomparison Project phase 6 (CMIP6) General Circulation Model (GCM) ensemble output. Radiocarbon data and multiannual volume transport through the Yucatan Channel suggest deep water residence times ~100 years for the GoM. Comparisons to previous radiocarbon observations suggest that the deep GoM has aged in the recent past, consistent with observed raising temperatures and the CMIP6 GCM simulations. The distribution of radiocarbon indicates a time frame of ~160 years between North Atlantic convection and complete ventilation of the deep GoM. This suggests that aging and warming of GoM deep waters were initiated in the North Atlantic before ~1890 consistent with reported rapid and persistent AMOC weakening since the Little Ice Age.

INTRODUCTION

Circulation in the Gulf of Mexico (GoM) is often described as a two-layer system. In the top 1000 m, it is influenced by the Loop Current, entering the GoM through the Yucatan Channel (YC) and exiting through the Florida Strait (FS), and by Loop Current Eddies (100 to 300 km wide) that separate from the Loop Current every 4 to 18 months and propagate westward until they dissipate near the western coast (*1*). The deep layer in the GoM (>1200 m) is characterized by cyclonic circulation patterns in the form of a western boundary current and a deep central cyclonic gyre, based on Sound Fixing and Ranging (RAFOS) float data (*2*), hydrocast and profiling float data (*3*), current meter mooring data (*4*), and numerical models (*5*).

The upper layer in the GoM consists of a variety of advected water masses entering the GoM from the Caribbean Sea including Caribbean surface waters, Subtropical Underwater (SUW), 18° water, North Atlantic Central Water (NACW), South Atlantic Central Water (SACW; the latter two are sometimes collectively referred to as Tropical Atlantic Central Water), and Antarctic Intermediate Water [AAIW (*6*, *7*); see water mass characteristics in table S1]. The deep layer in the GoM originates in the North Atlantic (NA) as Upper North Atlantic Deep Water (UNADW) believed to be predominantly Labrador Sea Water (*8*–*11*). More recent studies (*12*, *13*) have shown that UNADW partially originates in the Irminger and Iceland Basins. Deep waters enter the Caribbean Sea through the Windward Passage (1680 m) and the Anegada-Jungfern Passage (1820 m) and the GoM through the YC [2040 m; (*3*, *14*, *15*)]. Because of the different sill depths in the YC (2040 m) and the Straits of Florida (800 m), UNADW entering the GoM through YC does not exit the Gulf through the Straits of Florida. The ultimate source for the waters entering the Caribbean Sea and the GoM as part of the Loop Current is believed to be partially derived from the NA Subtropical Gyre circulation system and partially from the South Atlantic. The NA Subtropical Gyre source is driven by Sverdrup transport, while the South Atlantic source represents part of the compensating flow for NADW crossing the equator (*8*). The GoM is therefore connected to the NA by the upper (Gulf Stream) as well as the lower limb (UNADW) of the Atlantic Meridional Overturning Circulation (AMOC), and both are affected by recent climate change (*16*, *17*).

The general features of deep ventilation of the GoM have been known for more than 50 years (*18*), but many of the more recent global hydrographic programs, like the World Ocean Circulation Experiment (WOCE), the Climate and Ocean: Variability, Predictability and Change (CLIVAR) project and the Global Ocean Ship-Based Hydrographic Investigations Program (GO-SHIP), have not included the GoM. This is particularly true for tracer observations typically used to study deep ventilation. Current estimates for deep water residence times in the GoM range from <100 to >250 years (*6*, *19*, *20*). Consequently, the GoM is poorly understood with respect to deep ventilation time scales and its sensitivity to changes in the NA.

Understanding AMOC variability and response to climate change is particularly difficult. Observational studies favor decadal variability driven by changes in the North Atlantic Oscillation (NAO) index as the main reason behind hydrographic variability in the NA (*21*, *22*). Meanwhile, modeling studies suggest long-term AMOC trends driven by climate change (*16*, *23*). Observations rely on available data that go back to the 1950s (*10*, *21*, *22*, *24*). These

[1]Department of Marine and Coastal Environmental Science, Texas A&M University at Galveston, Galveston, TX, USA. [2]Department of Oceanography, Texas A&M University, College Station, TX, USA. [3]Centro de Investigación Científica y de Educación Superior de Ensenada (CICESE), Ensenada, Mexico. [4]Universidad Autonoma Baja California (UABC), Ensenada, Mexico. [5]Atmospheric and Oceanic Sciences, Princeton University, Princeton, NJ, USA.
†Deceased.
‡Present address: Department of Earth and Environmental Science, University of Pennsylvania, Philadelphia, PA, USA.
*Corresponding author. Email: amonr@tamu.edu

data cover a period of a pronounced negative NAO index with weak convection in the Labrador Sea during the 1960s and a period of pronounced positive NAO, with strong convection, during the 1990s. The transition from weak convection in the 1960s to strong convection in the 1990s may mask other longer-term changes over the past 200 years. Regardless of what causes the changes observed in the NA and the AMOC, we currently have little insight as to how this might affect the exchanges with the deep waters of the GoM or what kind of clues the variability within the deep GoM might hold to understand AMOC variability. The paleoceanography record suggests substantial variations in GoM′s deep water (GoMDW; depths >2000 m) chemistry over time with low nutrient concentrations during periods of a strong AMOC and high nutrient concentrations during periods of a weaker AMOC (*19*). The shift in GoMDW chemistry is explained by a varying contribution of UNADW relative to intermediate water sourced from the Southern Ocean (*19*). Such changes in northern and southern source water contributions to intermediate waters of the NA have been suggested on <100-year time scales (*25*). Shorter-term changes (past 20 years) have recently been observed in GoMDW temperatures indicating a steady increase below 2000 m over a 16-year time period (*26*).

To improve our understanding of the relationship between NADW formation and GoMDW properties and to establish a time frame for deep water circulation, we used a combination of existing and recent radiocarbon distributions of dissolved inorganic carbon (DIC) in the GoM and the Western Caribbean (Fig. 1) and volume transport estimates from the YC and FS (*27*). Existing radiocarbon data are limited to two depth profiles from 1978 (*28*) and 1993 (*29*) and a few profiles from the northcentral GoM collected in 2015 (*20*). Continuous simultaneous current measurements across the YC and the FS are also limited, so we use a time series collected between 2012 and 2016 (*27*). The observed trends in the deep GoM and deep-water transport times between the NA, the Caribbean Sea, and the GoM are then put in perspective to an ensemble of eight state-of-the-art Coupled Model Intercomparison Project phase 6 (CMIP6) General Circulation Models (GCMs) (table S2) (*30*, *31*) as well as the output from a Total Matrix Intercomparison (TMI) (*32*) to see whether our interpretation of observations is consistent with simulations and the climatology.

RESULTS

To understand the connections between the deep GoM and deep-water formation in the NA, we first need to understand the time frame. How long does it take for waters subducted in the NA until they reach and ventilate the deep GoM? This can be accomplished by combining several independent approaches, the radiocarbon distribution (including natural, anthropogenic, and nuclear bomb–derived radiocarbon), and volume transport based on recent current measurements. Hydrographic data and models can then be used to confirm observed changes and infer source contributions in Gulf of Mexico Deep Water (GoMDW).

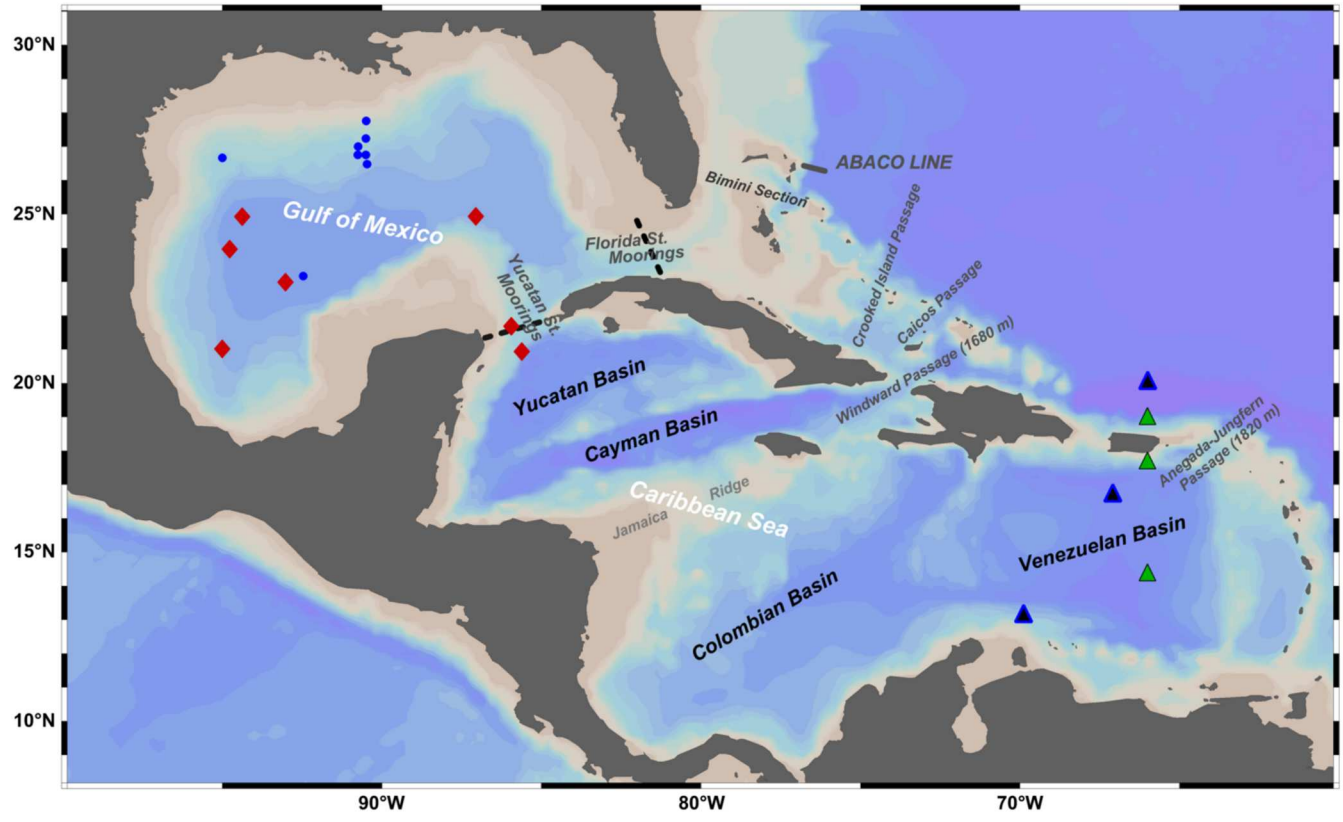

Fig. 1. Radiocarbon sampling locations during the 2017 CIGoM program (red diamonds). Also included are existing data from the GoM [blue dots; (*20*, *28*, *29*)] and from the WOCE and CLIVAR section A22 [green triangles; (*74*); black triangles; (*56*)]. Approximate positions of mooring arrays are indicated with black dotted lines.

Radiocarbon content

The radiocarbon content of GoMDW below 1200 m was very homogeneous, averaging −95.3 ± 1.8‰ (Fig. 2). In contrast, the various water masses above 1200 m in GoM are more heterogeneous in terms of radiocarbon values (Fig. 2 and table S1). Clear differences were observed between deep waters (>2000 m) of the Yucatan Basin in the Caribbean Sea and the GoM. GoMDW have more depleted $\Delta^{14}C$ values than Yucatan Basin deep waters (Fig. 2). In addition, recent radiocarbon data from western GoMDW (−96.3 ± 1.3‰; n = 7) are slightly depleted relative to deep waters at the eastern GoM station (−94.4 ± 1.8‰; n − 8) by about 2‰ (Fig. 2) or 15 years in radiocarbon age equivalent. This difference is small but was shown to be significant (Student's t test; $P \leq 0.008$). In contrast to GoMDW, the depths profiles in the Yucatan Basin show more variability, with enriched $\Delta^{14}C$ values around 2000 to 2500 m relative to the waters sampled above and below (Fig. 2). This is consistent with distributions of dissolved oxygen (see below), with the highest values at the depths of 2000 to 2500 m, indicating a more recent ventilation with UNADW. Deep water samples collected in the western YC (1200 to 1800 m) have similar radiocarbon and oxygen concentrations as those from the central GoMDW. This confirms that samples taken from ~1200 m in the western YC represent outflowing waters (leaving the GoM) rather than inflowing waters from the Caribbean Sea (Fig. 2). This is consistent with mooring-based current meter observations presented by Candela *et al.* (*27*).

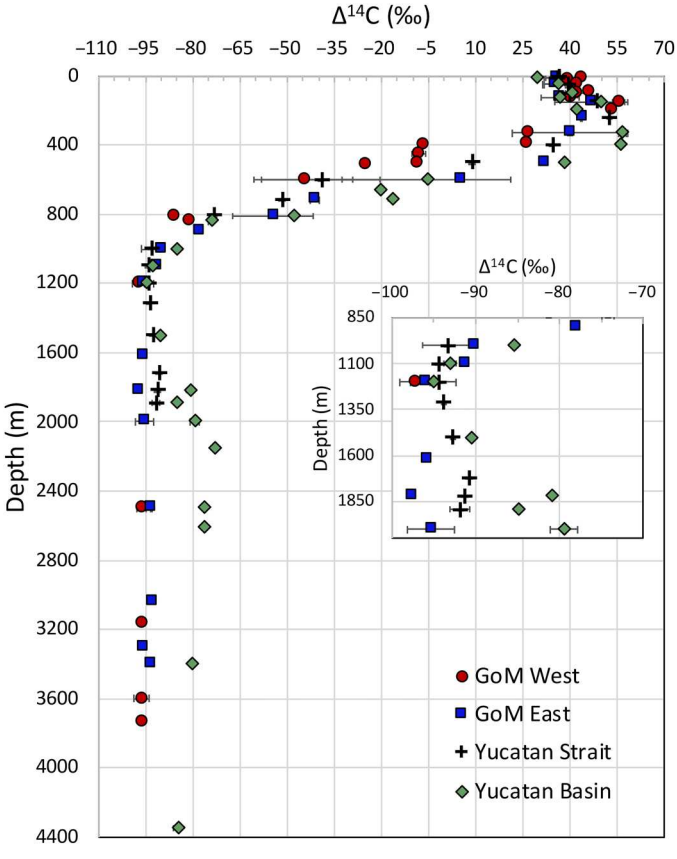

Fig. 2. Depth profiles of DI^{14}C from different locations in the GoM. Sample locations include the western and central GoM (red symbols; averaged), the easternmost station nearest to YC (blue squares), the YC (black crosses), and the Yucatan Basin in the Northern Caribbean (green diamonds). The strong radiocarbon gradient between 300 and 800 m represents the transition from NACW to SACW and AAIW. Inset expands the scale for mid-depth samples.

Radiocarbon-based residence times of deep waters in the GoM

North Atlantic Deep Water in the GoM and Caribbean Sea consists almost exclusively of UNADW (*9*, *14*) defined by a potential density >27.76 kg m^{-3} in the NA (*10*, *11*, *33*). The average $\Delta^{14}C$ value for GoMDW from this density range is −95.1 ± 1.8‰. This value is very distinct from UNADW (>1600 m) collected in 2017 and 2019 in the Yucatan Basin that averages −79.0 ± 3.6‰.

To interpret these differences with respect to conventional radiocarbon age and residence times, one must understand and correct for the contribution of nuclear bomb ^{14}C and fossil fuel–derived CO_2 (C_{ant}). Bomb ^{14}C would make a sample appear to be more enriched in $\Delta^{14}C$ (younger) than it actually is, while contributions of C_{ant} would make a sample appear more depleted in $\Delta^{14}C$ (older). Both can influence $\Delta^{14}C$ values in recently ventilated water masses (<100 years) and would result in erroneous estimates for radiocarbon ages and radiocarbon-derived residence times. C_{ant} and bomb ^{14}C enter the ocean as CO_2 from the atmosphere, but their atmospheric concentrations vary independently and their equilibration time is different (*34*). C_{ant} has an air-sea equilibration time of about 1 year and has been increasing exponentially in the atmosphere for more than 150 years. C_{ant} now represents roughly 30% of atmospheric CO_2. Bomb ^{14}C has an air-sea equilibration time on the order of 10 years and was added to the atmosphere over two decades starting ~1945, increased rapidly until 1965, and has been declining exponentially since then (*34*). At its peak in 1964, there was about twice as much radiocarbon in the atmosphere relative to the pre–nuclear-bomb background (up to +1000‰ in $\Delta^{14}C$ terms). Before the nuclear bomb signal, radiocarbon had been decreasing steadily in the atmosphere since ~1820 (*35*).

These differences influence the spatial distribution of bomb ^{14}C and C_{ant} in the oceanic DIC pool, which is currently not well constrained, particularly in deep waters. Therefore, we calculated the contributions of bomb ^{14}C and C_{ant} for the different deep-water masses in the GoM, the Yucatan Basin, the Venezuelan Basin, and in the NA (Fig. 3). Bomb-derived ^{14}C was estimated with the approaches suggested by Rubin and Key (*36*) and C_{ant} following the conservative tracer (ΔC^*) approach suggested by Gruber *et al.* (*33*) as modified by Lee *et al.* (*37*), as well as Touratier *et al.* (*38*). These estimates indicate that GoMDW currently does not contain bomb ^{14}C or radiocarbon-dead fossil fuel CO_2. In contrast, deep waters (≥2000 m) sampled in the northern Yucatan Basin, in source waters to the GoMDW, do show measurable bomb ^{14}C and anthropogenic CO_2 (Fig. 3). This indicates that these tracers are just arriving at the "gate" to the deep GoM. The uncertainty associated with these estimates is high, 15‰ for bomb ^{14}C (*36*) and 6‰ for C_{ant} (*37*). NA waters outside Anegada-Jungfern Passage and in the Venezuela Basin have measurable amounts of both tracers and show an increasing trend between 1997 and 2012 (Fig. 3). Druffel's (*39*) NA surface water coral data (near Bermuda) show the first appearance of bomb ^{14}C around 1962. Subsequently, the bomb ^{14}C values continued to increase until the mid-1980s (*39*).

Given the large uncertainties associated with bomb ^{14}C estimates (15‰), the opposing effects of bomb ^{14}C and C_{ant} are difficult to

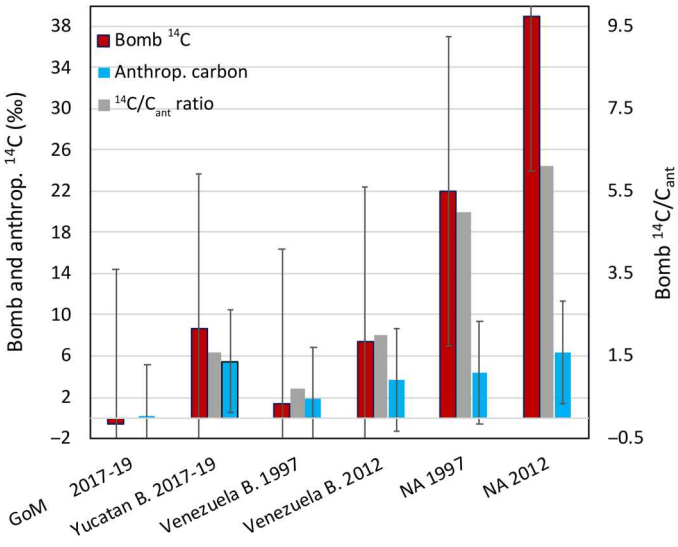

Fig. 3. Distribution of bomb ^{14}C and anthropogenic carbon (expressed in per mill equivalents, Eq. 11) along with the bomb ^{14}C/C$_{ant}$ ratio in the different ocean basins and over time. Values are averages for potential density anomaly >27.725 kg m^{-3} (to the sill depths of 1680 m at Windward Passage and 1820 m at Anegada Passage for inflowing NADW). Bomb ^{14}C is based on the relationship to silicate (*36*), and C$_{ant}$ is based on the approach of Lee *et al.* (*37*). Error bars represent the uncertainty given in the respective references, which are 15‰ for bomb ^{14}C and 6‰ for C$_{ant}$. The uncertainty for C$_{ant}$ was reported (*37*) as 8 μmol liter^{-1} and was converted to ‰ equivalents using Eq. 11. NA, North Atlantic Basin.

resolve for the Yucatan Basin. We therefore estimated the residence times for the deep GoM as the difference in radiocarbon ages between the deep waters of the Yucatan basin and GoM as well as based on the difference between the inflowing and outflowing waters in the YC with and without consideration of bomb radiocarbon or C$_{ant}$. The deep GoM (>2000 m) is ventilated by waters entering through the YC (*6*, *14*) between about 1800 m and the sill depth at 2040 m, characterized by a potential density σ_0 >27.755 kg m^{-3}. Conductivity, temperature, and depth (CTD) measurements in the vicinity of the YC sill show that the inflow at depths from ~1800 m to the bottom is composed of heavier waters than found anywhere near the bottom of the GoM interior (fig. S1). Dissolved oxygen concentrations also indicate that the basin fills partially from the bottom up and that deep water is eventually mixed upward (<2000 m) in the GoM and leaves through YC between 800 and 1500 m (*6*, *27*). The Yucatan Basin samples at this density range (>1600 m) had a Δ^{14}C value of −79.0 ± 3.6‰. This is enriched by 16.1‰ relative to average GoMDW (−95.1 ± 1.8‰) and represents a conventional radiocarbon age difference of ~135 years.

Another way to estimate deep water residence times is the comparison of conventional radiocarbon ages between inflowing "sill water" and outflowing intermediate water in the YC. Taking the deep water value from Yucatan Basin (−79.0 ± 3.6‰) as representative of inflow water and the 1200-m sample from the western YC (−94.4‰) as representative for outflowing deep water, the difference is ~131 years. If we correct the average deep Yucatan Basin value for bomb ^{14}C and C$_{ant}$, the Δ^{14}C is −82.1‰ and the age difference is ~108 years.

Following Broecker and Gerard (*40*) and assuming the mixture of two deep water reservoirs, we can also derive a mean residence time for the deep GoM using their equation

$$R_{GOM} = (\Delta_{CAR} - \Delta_{GOM})\tau/1000 \quad (1)$$

where R_{GOM} is the mean residence time of the deep GoM, Δ_{CAR} and Δ_{GOM} are the Δ^{14}C values of the deep northwestern Caribbean and the GoM, respectively, and is the mean life time of a ^{14}C atom (8033 years). On that basis, we estimate that it takes ~105 years to renew GoMDW (>2000 m). The uncertainty for these residence times is about 30 years for uncorrected and ±160 years for corrected radiocarbon data, due to the large bomb ^{14}C error of 15‰ (*36*).

Residence times based on current measurements and volume transport

An independent estimate of GoMDW residence time can be obtained from YC and FS volume transports. The YC has a sill depth of 2040 m, while the FS has a minimum sill depth at the Bimini section of 820 m (*41*). Therefore, we can assume that the fraction of waters that enter the GoM through the YC at levels deeper than ~1000 m and does not return through YC into the Caribbean Sea (>1000 m) must have substantial changes in their composition (i.e., by mixing and becoming lighter) to exit the GoM through YC and the FS. The outflow of deep waters through the FS is very limited because of its shallow depth (ca. 800 m), and most of the outflow takes place through the YC's eastern and western margins at depths of 800 to 1500 m. There must be net upwelling in the GoM's interior for this to happen, basically related to the continuous input of dense water through the YC sill and its mixing with lighter waters within (Fig. 4 and fig. S1).

The most recent and complete YC transport measurements were reported by Candela *et al.* (*27*). They presented 4 years (September

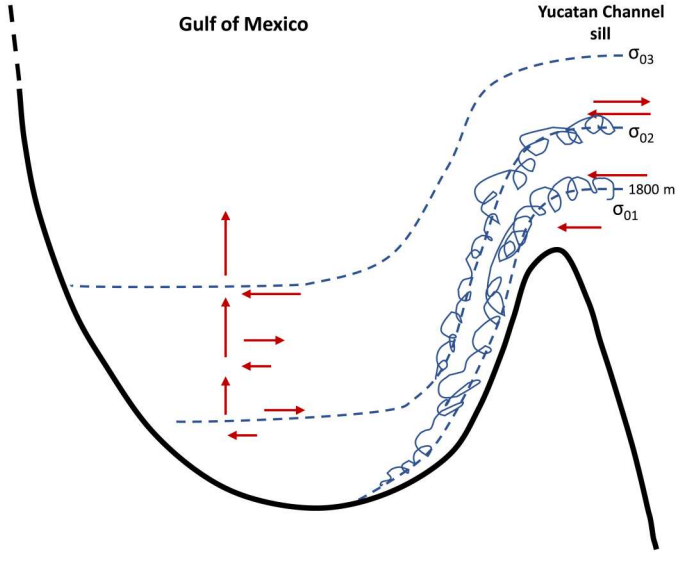

Fig. 4. Schematic drawing of mixing of dense overflow water with resident water in the GoM near YC. The downslope flow fills the deep waters within the gulf. Inflowing waters of density σ_{01} from ~1800 m to the bottom at the Yucatan sill are denser than anything found in the interior GoM. The isopycnal σ_{02} at ~1700 m at the sill is found on the bottom of the GoM, a vertical displacement of ~1800 m. Such mixing is evident in dissolved oxygen (DO) profiles in the eastern Gulf (fig. S4). The σ_{03} isopycnal represents a lighter density water than σ_{02}, which permits outflowing waters below it and diapycnal mixing with the waters above.

2012 to August 2016) of continuous current measurements from mooring-array sections across the channels (Fig. 1). They estimated mean volume transport on the basis of two slightly different interpolation procedures. The first was obtained by objectively interpolating the measured currents through the Yucatan and Florida sections over the entire 4-year period, at every hourly time step and exploring 72 different combinations of horizontal and vertical scales. The best match between Yucatan and Florida sections, both in mean transport and in time evolution, was using 80 km and 700 m (horizontal and vertical scales) for the Yucatan section and 80 km and 600 m for the Florida section, giving a mean transport of 27.6 Sv with annual variations of up to 3 Sv (their figures 3A and 5). Although the obtained mean currents section in Yucatan and Florida are reasonable, the deep counter currents in the Yucatan section are somewhat different from previous estimates. Because the interest here is mainly the deep flow, another way to calculate the mean current section was investigated. The second approach was obtained by interpolation of the current means from series in both channels that were longer than 1 year, under the premise that a year of measurements is a reasonable representation of the mean annual flow at a given depth. This yields a mean of 27.2 Sv for the period. Because both mean current patterns are plausible, we calculated deep water volume transport and residence time based on both approaches.

Figure 5 (A and B) shows the simplest mean profiles of volume transports below 1000 m based on the two transport estimates reported by Candela *et al.* (*27*). In both cases, the volume transport below 1000 m into the GoM is larger than the return to the Caribbean Sea. No appreciable return flow occurs below ~1500 m. To derive deep GoM residence times, we incorporate upward diapycnal mixing by either considering the inflow of water masses heavier than some reference density or the outflow of the same water mass to the Caribbean plus the outflow of diapycnally mixed water above the reference density. This can be expressed in a simple box model bounded by isopycnals (fig. S2). We consider a single inflow into the deep GoM through the YC and the outflows through the FS and toward the Caribbean and assume that the volume remains unchanged.

A schematic model for the deep Gulf ventilation is shown in Fig. 4. The mathematical expression of the simple box model is given in fig. S2 and associated text. Diapycnal processes must be large enough to compensate for the imbalance between horizontal outflow relative to the inflow (>1000 m). The residence time is derived by calculating the time it takes to fill/empty a certain volume below a reference density considering only the inflow into the volume. Figure 5 (C and D) shows the residence times for water masses denser than 27.6 kg m^{-3} and deeper than 1000 m. Focusing on depths below the YC sill (denser than 27.755 kg m^{-3} or >2000 m), the residence times average either 76 or 67 years based on the two approaches (Fig. 5). The total range of residence times below 2000 m for the GoM, based on the two volume transport estimates, is 30 to 105 years (Fig. 5, C and D). However, the lower estimates are based on the direct mean approach, which has much larger errors due to the reduced number of observations with >1 year of measurement periods at those depths. This increases the uncertainty in volume transport when focusing on the bottom layer of YC (*27*). The deep flow in YC seems to be captured more reliably using the matching transport approach between YC and FS represented by the black line in Fig. 5 (C and D). This results in a volume transport–based residence time for the deep (>2000 m) GoM between 75 and 105 years. The same dataset can be used to roughly estimate a mean inflow below 1800 m in YC of 0.22 Sv (*26*). Such volume transport would replace the volume of the GoM below 2000 m in 100 years. However, the variability of deep water volume transport in the YC might be several times larger than the mean flow resulting in an uncertainty for volume transport–based residence times in excess of 100 years (*27*). Despite the large uncertainty associated with each residence time estimate, based on radiocarbon or volume transport, the two independent approaches for deep GoM residence times converge at ~100 years.

Transport through the deep Caribbean Sea

Next, we need to understand how long it takes UNADW to be transported through the deep Caribbean Sea. $\Delta^{14}C$ values in the density range of UNADW decrease from the NA to the Caribbean and lastly the GoM. UNADW in the Venezuela Basin is slightly less depleted (−87.8 ± 2.9‰; based on 2012 data) than UNADW in the GoM in 2015–2017 (Table 1). UNADW in the Yucatan Basin is significantly more enriched (−79.0 ± 3.6‰) than in the deep Venezuela Basin. This indicates that the deep Yucatan Basin is predominantly ventilated through the Windward Passage and on shorter time scales than the Venezuela Basin or the GoM (see the Supplementary Materials), consistent with findings by Sturges (*18*).

Estimating deep water renewal in the Yucatan Basin is more challenging than for the GoM because of potential contributions from several deep water sources. Inflows from Windward Passage and across Jamaica Rise (~1550-m maximum depth) from the Colombian Basin are not well characterized in terms of volume transport. We can derive a rough residence time estimate by using the estimated bomb ^{14}C near the YC as an age tracer. First, we assume that bomb ^{14}C was initially introduced to the NA convection regions around 1962 (*39*). Elevated levels of bomb ^{14}C and C_{ant} relative to the deep GoM were observed near YC in 2017. Thus, it took ~55 years for the bomb ^{14}C signal to travel from the NA to sill depth of YC. The time it takes UNADW to get from the NA to the Abaco line (Fig. 1) along the Deep Western Boundary Current (DWBC) was estimated at 9 years (*42*, *43*). To reach Windward Passage from there, it takes three to five more years via Crooked Island and Caicos Passages (*44*) assuming the current velocity of 1.2 to 1.5 cm s^{-1} given by van Sebille *et al.* (*42*), but not more

Table 1. Average $\Delta^{14}C$ values and conventional ages in deep waters (>27.725 kg m^{-3}) of the different relevant ocean basins.

Geographical area (σ_0 27.725 to 27.795 kg m^{-3})	$\Delta^{14}C$ (‰)	Bomb ^{14}C (‰)	C_{ant} (‰)	Corrected ^{14}C age (years)
North Atlantic, near Anegada-Jungfern Passage (2012)	−44.0 ± 4.8	38.9	6.4	578
Venezuela Basin (2012)	−87.8 ± 2.9	7.4	3.7	706
Yucatan Basin (2017–2019)	−79.0 ± 3.6	8.6	5.5	626
GoM (2015–2017)	−94.7 ± 2.3	0	0	733

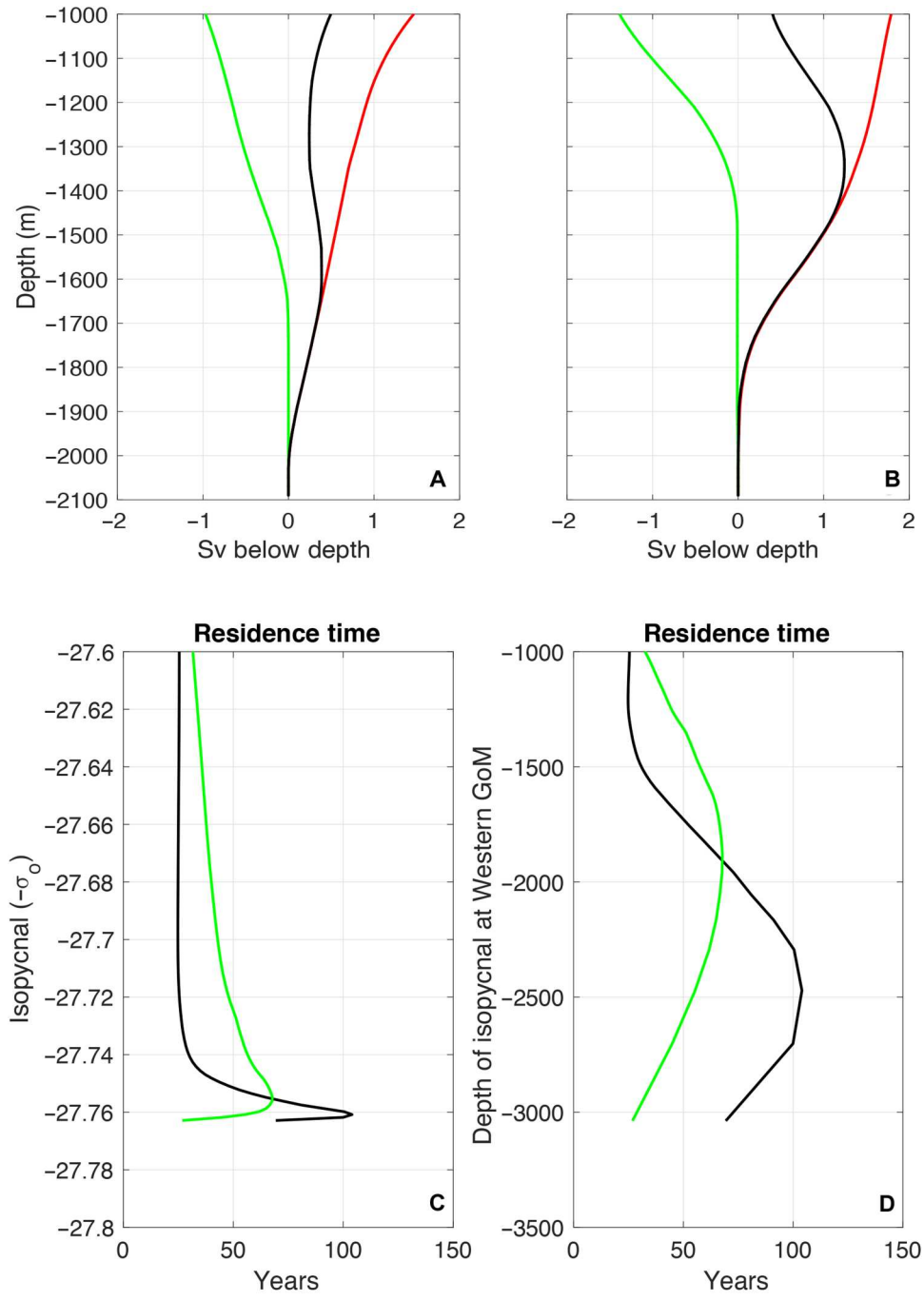

Fig. 5. Mean volume transport below the 1000m reference depth in the YC and derived residence times in the deep GoM. - Volume transport estimates are based on the 4-year observed current means (**A**) or based on the mean distribution matching the transport between YC and FS (**B**). In green is the contribution toward the Caribbean Sea, in red is the contribution into the GoM, and in black is the total transport. Residence time versus isopycnals (**C**) or depth (**D**) for the two mean current profiles obtained in YC by Candela *et al.* (*27*). The green line corresponds to the volume transport based on direct mean current measurements with more than 1 year of observations in YC (A), and the black line represents estimates derived from matching the volume transport in YS and FS (B).

than 15 years in total, consistent with tracer and model estimates (*45*, *46*). This implies that it took the UNADW bomb ^{14}C signal ~40 years to transit through the deep Cayman and Yucatan Basins from Windward Passage to YC. An independent, radiocarbon-based, residence time for the Yucatan/Cayman Basin can be derived using Eq. 1 (*40*) from above and the radiocarbon data given in Table 1. Using corrected radiocarbon data for the Yucatan Basin (this study) and the NA (2012), we derive a mean residence time of 45 ± 160 years. Assuming that these two independent estimates (transit time based on bomb ^{14}C and residence time based on natural ^{14}C) are representative for mean residence times of the combined Yucatan and Cayman Basins and a volume of 1×10^{15}

m^3 for the combined Yucatan and Cayman Basins below 1700 m (Windward Passage sill depth), we can calculate an average Windward Passage deep water inflow of 0.65 to 0.75 Sv, which is within the range of reported values (*44*). Because only 0.3 Sv will leave the Yucatan/Cayman Basins toward the GoM (*27*), a substantial fraction of Windward Passage deep inflow must flow into the Colombian/Venezuelan Basin or return to the Atlantic through the Windward Passage. The outflow toward the Colombian Basin deep waters is consistent with higher dissolved oxygen concentrations in the Colombian Basin relative to the Venezuela Basin (*47*; World Ocean Database 2018; see the Supplementary Materials for details on Venezuela Basin ventilation).

Dissolved oxygen in the GoM and adjacent basins

The dissolved oxygen distributions seen in the deep waters of the different basins (Fig. 6) are consistent with each other and the inferred ventilation pathway. Atlantic deep water has the highest dissolved oxygen concentration (up to 260 μmol kg^{-1}), and GoM and Venezuela Basin deep water have the lowest (~205 and ~ 215 μmol kg^{-1}, respectively; Fig. 6). Yucatan Basin deep water values are higher (~232 μmol kg^{-1}) than in the Venezuela Basin and fall between the NA and the Venezuela Basin deep water values. The Yucatan Basin dissolved oxygen concentrations are much higher than in the deep GoM. This supports the earlier contention that Yucatan Basin deep waters must be ventilated by UNADW through Windward Passage. This is corroborated by the distribution of oxygen and potential density in the different basins (Fig. 6). Density follows the same pattern as dissolved oxygen with the highest density in UNADW in the Atlantic, followed by Yucatan Basin Deep Water and Venezuela Basin Deep Water, and the lowest density in GoMDW (Fig. 6). The density of UNADW flowing across the sill depths of the Windward Passage (1680 m) and the Anegada-Jungfern Passage (1820 m) is high enough to ventilate the Yucatan/Cayman and Venezuela Basins to the bottom. The same is true for the density in the Yucatan Basin near the YC sill depth (2040 m), which is dense enough to ventilate the deep

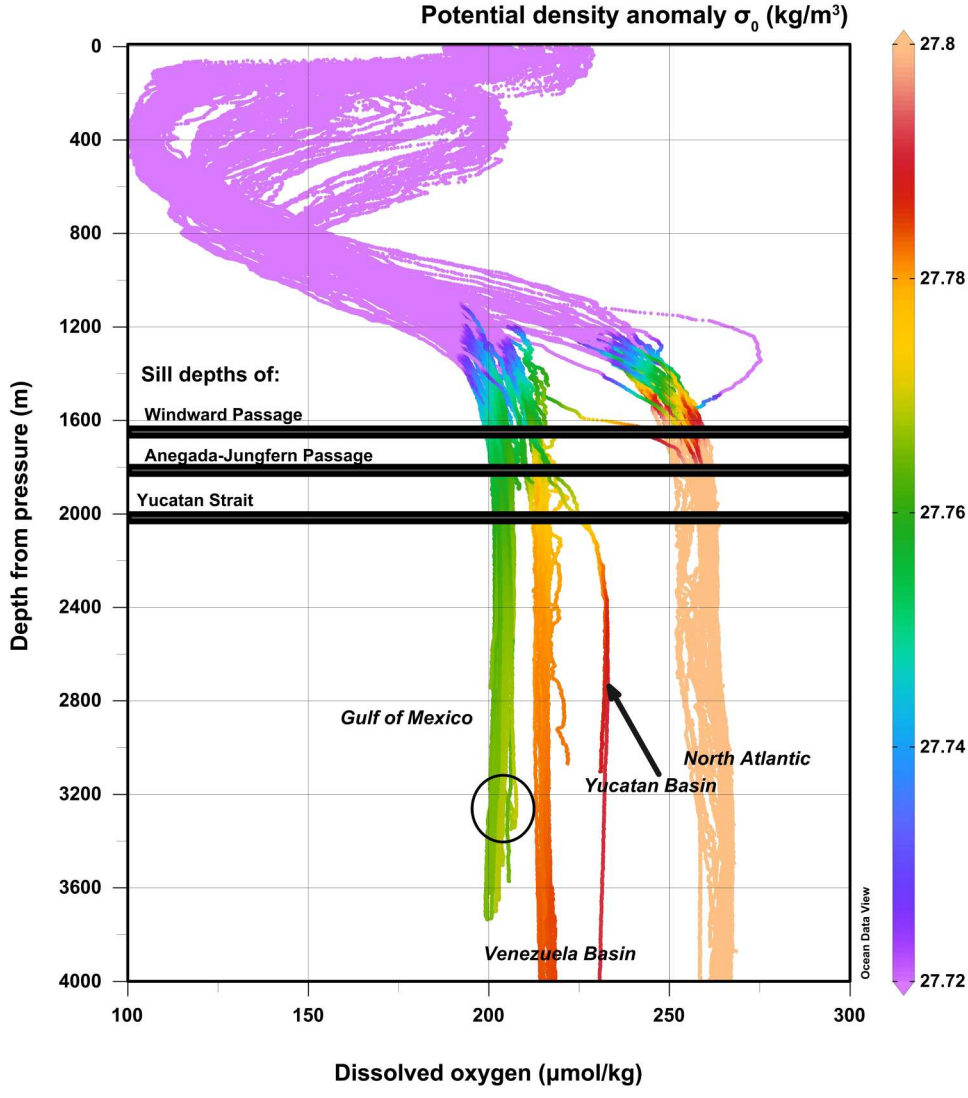

Fig. 6. Depth profiles of DO in the different basins along with potential density anomaly in color. The horizontal black lines indicate sill depths of the Windward Passage, the Anegada-Jungfern Passage, and the YC. The black circle highlights the bottom oxygen maximum at the easternmost station (A10) in the GoM.

GoM to the bottom (Fig. 6 and fig. S1). This deep ventilation is reflected in a visible increase of dissolved oxygen near the bottom at the most eastward station in the GoM (marked with a circle in Fig. 6) and in a few stations in the Venezuela Basin (Fig. 6).

$\Delta^{14}C$ and dissolved oxygen values show that the main pathway for deep GoM ventilation is through the Windward Passage–Cayman Basin–Yucatan Basin connection and is therefore closely connected to processes in the NA. Combining the transport times established above, 15 years from the NA convection regions to Windward Passage, ~45 years from Windward Passage to the YC, and about 100 years to ventilate the deep GoM, we get a timeline of ~160 years. Hydrographic and geochemical changes currently observed in GoMDW must have been initiated in the NA more than ~130 years ago to be manifested in GoMDW (assuming three-fourths of the 100-year residence time of GoMDW and 60 years of transit time between the NA and YC). This raises the question of to what extent the observed variations in the AMOC (*22*, *24*, *43*) as well as changes in salinity, temperature, and oxygen identified in the DWBC (*22*, *42*) manifest themselves in the deep GoM. In other words, what can observed changes in the deep GoM tell us about upper NADW formation and AMOC variability in the past 200 years?

Recent changes in the deep GoM

Because the GoM was not included in hydrographic programs over the past decades, we currently do not understand the temporal variability to the degree we understand the hydrographic variability of the NA. A recent study (*26*) presented deep water temperature observations in the GoM indicating a warming trend over the past two decades. To determine whether such temporal changes are also observable in the radiocarbon record of GoMDW, we compared older radiocarbon data from the central GoM (*28*, *29*) to the recent data (2015–2019; Fig. 7). There is clearly more variability in the older radiocarbon data than in our recent dataset. The 1978 profile has one data point at 3000 m with $\Delta^{14}C$ value of −105‰, ~150 years older than the sample collected only 300 m below (Fig. 7). Such a large difference between two closely spaced samples is unlikely considering a deep water residence time of ~100 years. In addition, this specific data point is a clear outlier in the DIC $\Delta^{14}C$–oxygen relationship (fig. S3, point shown in red). Removing this particular value in our analysis of temporal changes results in an average deep water (≥1600 m) $\Delta^{14}C$ value of −91 ± 2.1‰ for the older data (1978) and −94.7 ± 2.3‰ for recent data. This represents a statistically significant difference (Student's *t* test; $P < 0.001$; assumptions of normality and homogeneity of variance were met) and suggests that GoMDW is ~30 years older now than in 1978–1993. Considering the 2017 samples from the southwestern Gulf only, which were sampled close to the 1978 station (Fig. 1), the difference in radiocarbon and conventional radiocarbon age between the older and recent dataset increases to 5.6 ± 3.6‰ and ~45 ± 30 years, respectively.

Connections to Atlantic deep water sources based on model simulations, observations, and climatology

To interpret observed deep water changes in the GoM correctly, it is critical to understand the connections between the NA and the GoM in terms of deep water origin and variability. Are the observed changes in temperatures (*26*) and radiocarbon ages produced within the GoM, or are they "imported" from the Atlantic? Ochoa *et al.* (*26*) discarded that geothermal heat flux is a potential source of the warming in GoMDW and suggested that warming source waters to the deep GoM must be the reason.

GCMs (*48*–*51*) do suggest that anthropogenic forcing has reduced NADW formation. Under climate change scenarios, the NADW formation decreases in GCMs, resulting in a slowdown of AMOC (*48*, *49*), including the UNADW component that ventilates the deep Caribbean Sea and GoM. The slowdown of deep water formation leads to a warming signal in the deep ocean in GCMs (*50*, *51*). The onset of AMOC slowdown in GCMs also results in slower ventilation times of deep waters, which leads to decreased DO levels in the deep ocean (*50*).

To see whether the connection between climate change driven AMOC slowdown and deep waters, suggested by modeling studies (*50*, *51*), can affect the deep GoM, we analyzed temperature and dissolved oxygen concentration output from eight latest-generation CMIP6 GCMs (table S2) (*31*, *32*) under historical and Shared Socioeconomic Pathways 8.5 (SSP8.5) higher-emission scenarios (*52*) for the 21st century in GoMDW (Fig. 8). The simulated ensemble average temperature change for the 2003–2019 period is 8.5 m°C per decade. This is less than what was recently observed [18.6 ± 2 m °C decade^{-1}; (*26*)] for the same time period. This can be attributed to the fact that the historical scenario is initiated in the year 1850 and does not capture AMOC changes due to the transition from the Little Ice Age. The warming trends that we calculated for GoMDW also resemble average trends for benthic waters in CMIP5/CMIP6 ensemble runs, showing similar timing of the warming onset around the year 2000 (*50*). However, the model ensemble also predicts an increase in the rate of temperature change toward the second half of the 21st century (Fig. 8A). For the period 2060–2100, the model ensemble shows a simulated rate of average temperature increase of ~15 m°C per decade, which is similar to what was measured in the GoM over the past decade (*26*). The models also predict a decrease of dissolved oxygen concentrations in GoMDW for the same time period, consistent with the observed aging trend of GoMDW (Fig. 8B). The timing of modeled climate change signals, like temperature and oxygen in GoMDW, are consistent with other global studies (*50*, *51*) and thus appear to be linked to the changes in AMOC, specifically its slowdown under projected climate change scenarios.

A weakening of AMOC, specifically UNADW formation, might change the contribution of different intermediate water masses coming into the Caribbean Sea and the GoM, causing the observed shift in GoMDW properties. To constrain the surface origin of GoMDW, we used the TMI approach (*32*) that is based on an inversion of tracer conservation equations using the climatology of six tracer fields (potential temperature, salinity, nitrate, phosphate, oxygen, and stable oxygen isotopes) that are used to generate a global ocean circulation pathway matrix with a 4° × 4° horizontal resolution and 33 vertical layers. According to the TMI, water from the deep GoM (3500 m) originates mostly from the NA (>71%) but also shows a substantial contribution from the South Atlantic (~25%) with the NA component being dominated by an Irminger Sea contribution (>41%), a substantial contribution (~19%) from the Greenland Sea, and a relatively smaller contribution (~4.7%) from the Labrador Sea (fig. S4). The importance of the Irminger Sea as a source region of UNADW in the DWBC has been shown on the basis of recent observations (*12*, *13*). The contribution from the South Atlantic is less clear but could be supplied by Upper

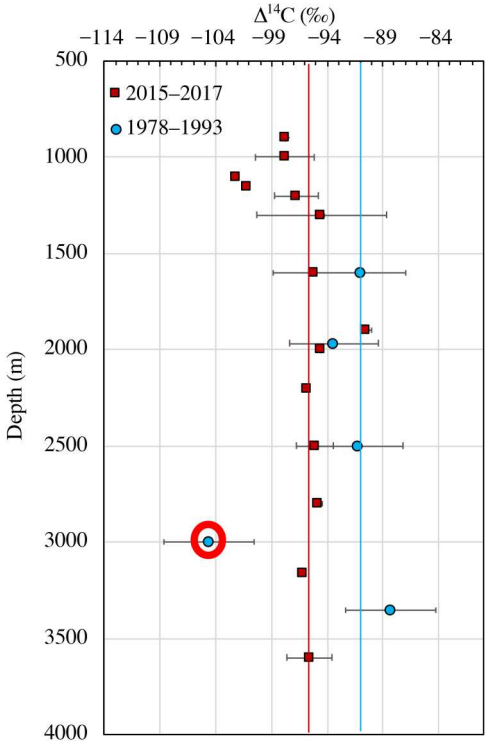

Fig. 7. Depths profiles of recent (red squares, 2015 and 2017–2019) and older (blue circles, 1978) radiocarbon measurements in the GoM. The red circle around the 3000-m data point in the historical profile is excluded from Student's *t* test (see main text).

Circumpolar Deep Water (UCDW) formed in the Southern Ocean with the same density characteristics as UNADW. This water mass is advected north in the Atlantic Ocean but is very difficult to trace hydrographically (*53*). A change in the proportions of UNADW and UCDW from the South Atlantic coming into the deep Caribbean Sea can explain the observed shift in GoMDW properties.

On the basis of the timeline outlined above, GoMDW discussed in this study (1978–2019) was last at the NA surface between 1820 and 1950. During this period, the radiocarbon levels in the atmosphere (based on tree-ring analysis) declined by about 30‰, partially because of variations in the cosmic ray flux, but mostly because of the increasing contributions from fossil fuel combustion (*35*). The radiocarbon depletion observed in the 1820–1950 atmosphere is also found in NA surface water mollusks shells [(*54*); as a proxy for surface water DI^{14}C] with a smaller long-term decline of 12‰. These changes generally agree with the radiocarbon depletion observed in GoMDW between 1978 and 2017. However, the observed 5.3‰ depletion in GoMDW radiocarbon is too large to be explained by a ~5.0‰ decline in NA surface water mollusk shells or a ~6‰ decline in the atmosphere, because only about half of the deep water in the GoM would be replaced in a 40-year period. This suggests additional factors are contributing to aging GoMDW.

The most likely reason for the observed decrease in radiocarbon of GoMDW is a larger South Atlantic contribution and mixing of UNADW with "older" intermediate water masses from the south, leading to a shift in radiocarbon content of waters crossing the sill in the Windward Passage. The observed gradients of NA radiocarbon (and other hydrographic parameters) near the Caribbean Sea is large enough within the general depth range (1200 to 1700 m) of incoming UNADW (*55*, *56*) to allow for the observed changes in radiocarbon and temperature (*26*), but observations in this region of the NA have a poor spatiotemporal resolution and do not cover the relevant time period. Because GoMDW is very homogeneous with respect to radiocarbon and has an estimated average residence time of ~100 years, the observed shift in radiocarbon and temperature (*26*) requires a long-term change in water mass characteristics coming in from the Atlantic, beyond the observed annual to decadal variability in the NA.

Annual and decadal changes in temperature and salinity have been reported for UNADW between the NA and the Abaco line at 26°N (*42*, *57*) and in the wider NA convection region (*10*, *22*, *24*, *43*, *57*). While some studies show a pronounced decadal variation of UNADW temperatures between 1960 and 2000 (*57*, *58*), Levitus *et al.* (*59*) indicate a continuous warming trend for most of the NA (down to 2000 m) since 1955. None of these observed changes in the NA would, however, be visible in GoMDW at this point based on the here presented timeline. This is particularly obvious in a recent study presenting a time series (1854 to present) of temperature changes and ocean heat content in the different depth layers of the AMOC system at 25°N (*60*). This study indicates that the layer between 700 and 2000 m at that latitude did show a slow gradual increase in temperature between 1850 and 1940 but a much more pronounced increase after ~1960. The same study also indicated that different components of the lower limb of AMOC respond differently over time with temperature increases being greater and starting sooner in UNADW, while the deeper components of AMOC (Iceland-Scotland Ridge Overflow and Denmark Strait Overflow) show a weaker and later temperature increase (*60*). A weakening of the UNADW formation in the Irminger-Labrador Sea region, at least over the past 70 years, was recently demonstrated on the basis of density observations and an ocean reanalysis (*61*). It is conceivable that here presented changes in GoMDW are likely caused by a weakening of UNADW formation allowing more older and warmer intermediate water from the South Atlantic to enter through Windward Passage along with UNADW.

The emerging ventilation scheme (Fig. 9) indicates that GoMDW is renewed about every 100 years by waters from the Yucatan Basin that originate mostly from the NA and enters the Caribbean via Windward Passage (*14*, *18*) as UNADW. GoMDW seems to be ventilated relatively evenly between 1200 m and the bottom as indicated by homogeneous Δ^{14}C depth profiles. Because oxygen concentrations of incoming Yucatan Basin waters are higher than within the GoM (Fig. 6), oxygen can also be used as a ventilation tracer in the GoM. Multilayer lateral mixing is implied in oxygen depth profiles of the easternmost station (fig. S5) where "bulges" were measured at several depth levels between 1200 m and the bottom. The zonal Δ^{14}C distribution reflects ventilation from the east, with a gradient of about 2‰ or 16 years between the western and eastern GoMDW. Deep ventilation to the bottom near the Yucatan sill is episodic (as seen in some dissolved oxygen depth profiles) and is clearly expressed as elevated dissolved oxygen levels in bottom waters. The high oxygen levels in YC sill waters are found at the bottom of the easternmost GoM station (A10; fig. S5) below 3000 m (Fig. 6). From there, elevated bottom oxygen can be traced northward to the Sigsbee Escarpment slope, then westward following a deep cyclonic boundary flow adjacent

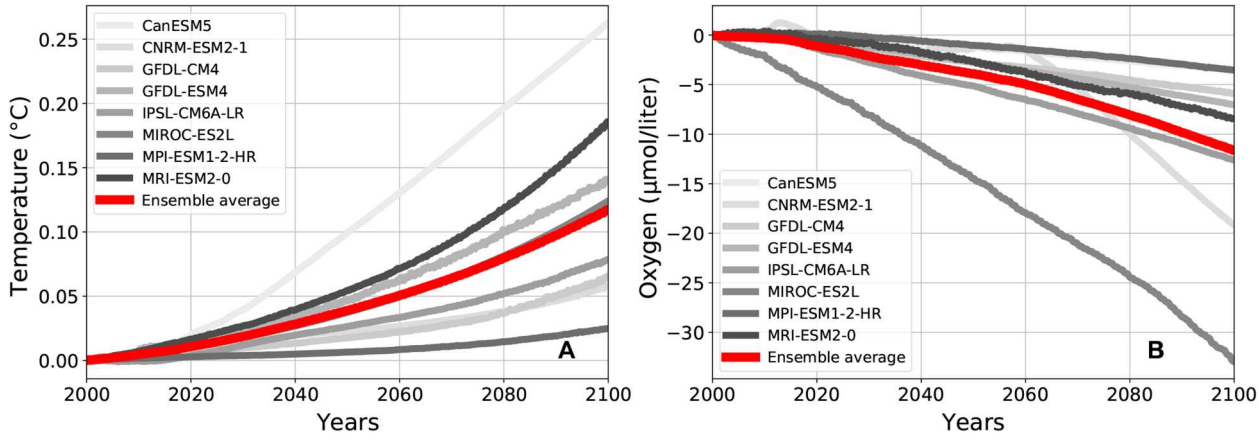

Fig. 8. Simulated temperature and oxygen changes in GoM deep waters between 2000 and 2100. Output from an ensemble of eight CMIP6 GCMs under historical and SSP585 scenarios for the 21st century.

to the slope (Fig. 9 and fig. S6). This circulation is consistent with the flow observed with current-meter moorings and float data and predicted by numerical models (Fig. 9) (*2*, *4*, *15*, *62*). Eventually, waters deeper than 2000 m are replaced by denser water from the YC sill and in turn get mixed into the intermediate layers (1000 to 1500 m) and exit the GoM through YC (Figs. 4 and 9) as suggested in the volume transport section and by Rivas *et al.* (*6*) and Sturges (*14*).

UNADW from the NA reaches the deep GoM after ~60 years and thus changes observed in the deep western GoM reflect changes in the NA that happened about 130 years ago. Because the combined transit time to and finally through the deep GoM is about 160 years (Fig. 9), and UNADW is entrained and mixed throughout two deep water basins sequentially, one would expect any annual-decadal NA variability signal to be diminished. We therefore think that only centennial-scale changes of NA convection are observable in the deep GoM. Support for this comes from paleoceanography. Buerkert (*19*) explained changes in GoMDW properties by NADW variations, with low nutrients during a period of strong NADW formation and high nutrients during a period of weaker NADW formation and a larger contribution from the south Atlantic. This is evidence that AMOC (UNADW) variability has influenced the properties of GoMDW in the past, however, on much longer time scales than studied here. Substantial subcentennial variability has been demonstrated for mid-depth (~1700 m) radiocarbon content in western NA deep-sea corals. Robinson *et al.* (*25*) related the deep-sea coral radiocarbon variability to changes in DIC caused by the varying contributions of northern and southern source waters, known as the "seesaw" pattern, during the last deglaciation. A similar process could be at work right now on an even shorter time scale by altering the relative contributions of UNADW and UCDW from the south coming into the deep Caribbean Sea and GoM.

DISCUSSION

Two independent approaches estimated the residence time of GoMDW at ~100 and ~45 years for the deep Yucatan/Cayman Basin. Despite the large uncertainties associated with each estimate, the fact that both approaches (radiocarbon and volume transport) produced very similar values instills a lot of confidence in these residence times. Considering a ~15-year transition time between the NA convection regions and Windward Passage, 45 years for water to flow through the deep Cayman/Yucatan Basin and ~75 years to replace three-fourth of GoMDW, we can estimate that it takes about 130 years before one can observe NA changes throughout the water column in GoMDW. The connection between NADW formation and GoMDW properties not only was consistent with a CMIP6 GCM ensemble and the TMI method estimating that current GoMDW consists of waters that originated (130 to 160 years ago) in the Irminger Sea (41%), the Greenland Sea (19%), and the Labrador Sea (5%) but also had a substantial (25%) contribution from the south, potentially UCDW (fig. S4) (*53*).

Our observations indicate a decrease in $\Delta^{14}C$ between 1978 and 2017/2019, and a temperature increase in GoMDW has recently been observed (*26*) for the period 2003–2019. On the basis of our timeline, these changes observed in GoMDW must have been initiated in the NA well before 1900 and before the observational record. Consistent with these observations, the latest generation of CMIP6 GCMs also indicate an increasing trend in temperature for the 21st century and suggests a declining trend for dissolved oxygen in GoMDW (Fig. 8). Assuming that dissolved oxygen can be used as a proxy for water mass age (time since ventilation), the observations and the model output suggest that GoMDW is aging and getting warmer. The explanation for these changes seen in GoMDW are likely rooted in the NA and climate change. Although a decrease in $\Delta^{14}C$ is also evident in the preindustrial atmosphere (*35*), it is unlikely that a 5‰ decrease in atmospheric and surface water $\Delta^{14}C$ (*35*, *54*) is transmitted 1:1 into the deep GoM given the 100 year "flushing" time. It is more likely that weakening of the UNADW component of the lower limb of the AMOC has resulted in diminished convection of cold and recently ventilated NA surface waters and a larger contribution of Southern Ocean waters. Such a process is consistent with more depleted $\Delta^{14}C$ values, higher temperatures, and lower dissolved oxygen in GoMDW. This proposed connection suggests that the NA and UNADW formation have been affected by climate change since the mid-19th century, long before our observational record. Caesar *et al.* (*23*) proposed such a long-term declining AMOC trend beginning ~1880, and Rahmstorf *et al.*

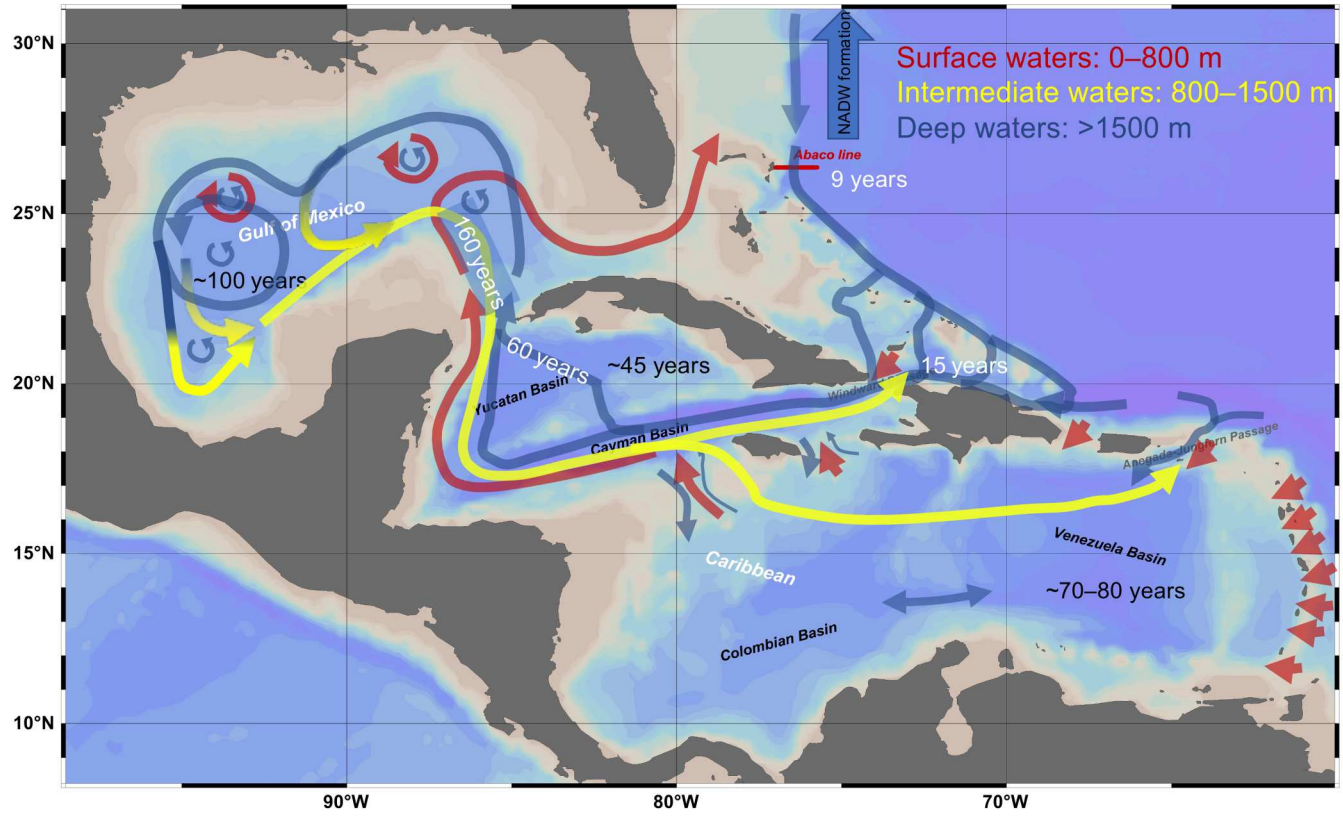

Fig. 9. Schematic for the general flow patterns of surface, intermediate, and deep waters in the GoM/Caribbean basins. White numbers indicate years since formation in the North Atlantic. Black numbers indicate the approximate deep waters residence times in the different basins.

(*16*) predicted it to continue under the current global warming trend.

Many of the decadal variability studies of NA convection and AMOC have been linked to the NAO index (*22*, *24*, *61*). The observational record starts after the second world war in the late 1940s and is characterized by particularly negative NAO index values into the 1960s. This causes weak convection in the NA. Very positive index values in the 1990s correlate with strong NA convection. Such changes in convection as well as other annual to decadal variability observed in the NA has not reached the deep GoM based on the proposed time line and can therefore not explain the observed changes in GoMDW. We think that the deep GoM acts as a "cul-de-sac" for UNADW, recording changes in the upper deep AMOC component that are integrated over multidecadal to centennial time scales and devoid of the annual to decadal variability that plagues the observational record from the NA. This view is in line with recent paleo-reconstructions of the past 150 to 300 years that indicate a major shift in NA hydrography (*63*) and a rapid weakening of the DWBC (*64*) around 1880 after the Little Ice Age. If the upper component of the lower AMOC limb has weakened on average since the mid-19th century, the observed trends in GoMDW will continue and should be recorded in cold water corals of the deep GoM and Caribbean Sea putting these locations at center stage to reconstruct AMOC changes over the past 200 years. With the existing observations, it is difficult to prove unequivocally that observed changes in GoMDW radiocarbon and temperature are linked to long-term AMOC weakening, but they are consistent with the CMIP6 GCMs, the paleorecord (*19*, *54*, *63*, *64*) and other modeling studies (*16*, *17*, *23*, *65*) covering the past few hundred years.

MATERIALS AND METHODS

Water samples were collected as part of the Mexican CIGOM project during cruises aboard the *R/V Pelican* and the *B/O Justo Sierra* between May 2017 and July 2019. Stations covered the southern (≤25°N) GoM and the Northern Yucatan Basin in the Caribbean Sea (Fig. 1). We collected water samples from the seven stations indicated in Fig. 1 at ~10 depths representing different water masses.

Targeted water masses included surface waters (<130 m), SUW, 18°C water, NACW, SACW, AAIW, and several depth levels of UNADW defined by potential density anomalies between 27.6 and 27.8 kg m^{-3} (see table S1 for depth ranges and hydrographic properties). Hydrographic data were collected with a Seabird CTD (911 plus). Water samples were collected using 12- or 20-liter Niskin bottles mounted on a 12-position rosette (General Oceanics). Water samples for radiocarbon analysis were collected and preserved following the UC Irvine protocols, and samples were analyzed at the UCI Keck Carbon Cycle AMS Laboratory. The analytical variability for radiocarbon analysis was ~1.8‰ for surface samples and 1.5‰ for deep water samples (≥1200 m). This was similar to the SD (±1.5‰) calculated for all (n = 11) deep water samples collected in the central GoM (≥1200 m). Total sample

measurement variability is reflected in the sample SD, including the variability introduced because of sampling and because of the analytical or counting error. DIC and alkalinity were determined at the Autonomous University of Baja California, using a coulometric method described by Johnson *et al.* (*66*), and a titration method described by Hernández-Ayón *et al.* (*67*). Reference materials were provided by the laboratory of A. Dickson of Scripps Institution of Oceanography. The accuracy obtained with respect to the reference material was ±2 μmol kg^{-1} with a precision of ±1.5 μmol kg^{-1}. Nutrient analysis was performed with an automated AA3-HR (Seal Analytical) nutrient analyzer following guidelines described in the GO-SHIP Repeat Hydrography Manual (*68*). Nitrate + nitrite and silicic acid were determined according to a modification of the Armstrong *et al.* (*69*) procedure. Reference materials for nutrients in seawater, lot CC and lot CD developed by the General Environmental Technos Co. Ltd. (Kanso Technos), Japan (*70*), were repeatedly analyzed during runs to evaluate accuracy and precision. The limit of detection for nitrate + nitrite and silicic acid concentration was 0.022 and 0.035 μmol kg^{-1}, respectively. Oxygen sensor data were corrected for sensor drift using ship board Winkler titrations.

Bomb-derived ^{14}C was estimated with the approaches suggested by Rubin and Key (*36*) based on silicate and potential alkalinity (PALK) using Eqs. 1 and 2. The two approaches agreed fairly well in deep water samples as far as the trend among different basins is concerned. Absolute values based on the silicate approach were consistently higher than values based on potential alkalinity.

$$\text{Bomb}^{14}\text{C}_{(\text{Si})} = \Delta^{14}\text{C}_{\text{Measured}} - [-70 - (\text{Silicate})] \quad (2)$$

$$\text{Bomb}^{14}\text{C}_{(\text{PALK})} = \Delta^{14}\text{C}_{\text{Measured}} - [-59 - 0.962 \times (\text{Alkalinity} + \text{Nitrate}) \times (35/\text{Salinity}) - 2320] \quad (3)$$

Anthropogenic CO_2 (C_{ant}; fossil fuel–derived CO_2) was estimated with the approach suggested by Touratier *et al.* [Eq. 5; (*38*)] and the ΔC* approach suggested by Gruber *et al.* (*33*) with modifications to the equations based on Lee *et al.* [Eqs. 6 to 10; (*37*)]. The per mill equivalent of the C_{ant} (micromole per kilogram) was calculated using a two-end-member mixing model, assuming a $\Delta^{14}C$ value of −1000‰ for anthropogenic, fossil fuel–derived CO_2, and the natural $\Delta^{14}C$ of DIC was calculated on the basis of Eqs. 4 and 11

$$\text{Natural } \Delta^{14}\text{C (‰)} = -70 - (\text{Silicate}) \quad (4)$$

$$C_{ant} = \frac{DO + 1.279^*(DIC - \frac{1}{2}^*A_T) - e^{7.511 - 0.01087 \times \Theta - 7.81x10^5/{A_T}^2}}{1.279} \quad (5)$$

$$C_{ant} = \Delta C^* - \Delta C^{DISEQ} \quad (6)$$

$$\Delta C^* = DIC^{meas} + {R_{C:DO}}^*(DO^{EQ} - DO^{meas}) - 0.5 \times [({A_T}^{meas} - {A_T}^\circ) - (DO^{EQ} - DO^{meas})]DIC^{EQ} \quad (7)$$

$${A_T}^\circ = 335.7 + 55.8 \times S + 0.08924 \times NO \quad (8)$$

$$NO = DO - R_{DO:N} \times NO_3 \quad (9)$$

$$DIC^{EQ} = 2077 - 8.517 \times (\Theta - 9) + 3.523 \times (S - 35) + 0.6399 \times ({A_T}^\circ - 2320) \quad (10)$$

$$C_{ant}(‰) = (\text{Fraction } C_{ant} \times -1000) + [\text{Fraction}(DIC - C_{ant}) \times \text{Nat.}\Delta^{14}C] - \text{Nat.}\Delta^{14}C \quad (11)$$

where C_{ant} stands for anthropogenic carbon, DO stands for dissolved oxygen, DIC is total DIC, and A_T and ${A_T}^\circ$ are total alkalinity and preformed alkalinity, respectively. We used micromoles per kilogram as unit for all these parameters. ΔC* is a quasi-conservative tracer introduced by Gruber *et al.* [Eq. 6; (*33*)], and ΔC^{DISEQ} is the air-sea CO_2 disequilibrium. We used the ΔC^{DISEQ} value for Labrador Sea Water at the 36.85 kg m^{-3} isopycnal (σ_2) given by Lee *et al.* (*37*). MEAS refers to the measured concentrations in water samples, DO^{EQ} is the saturation concentrations of dissolved oxygen, and DIC^{EQ} is the DIC concentration in equilibrium with a preindustrial atmospheric CO_2 concentration of 280 parts per million at salinity (S), potential temperature (Θ), and ${A_T}^\circ$. $R_{C:DO}$ and $R_{N:DO}$ are stoichiometric ratios relating inorganic carbon and nitrate (N) to dissolved oxygen (DO), respectively and are based on Anderson and Sarmiento (*71*). NO is a conservative tracer (*72*) and was derived using a $R_{DO:N}$ of 10.625 based on Anderson and Sarmiento (*71*).

The uncertainties were adopted from the referenced publications and were 15‰ for bomb ^{14}C (*36*) and ~6‰ for anthropogenic CO_2 (*33*, *37*). The 6‰ for C_{ant} are based on a total uncertainty of 8 μmol of C_{ant} (*37*). This adds very large uncertainties (~130 years in conventional radiocarbon age) to all residence time estimates based on bomb ^{14}C–corrected radiocarbon. We used published data on DIC radiocarbon, alkalinity, nutrients, and dissolved oxygen (if available) from the GoM/Caribbean Sea region from Ribbat *et al.* (*73*) Morrison *et al.* (*28*) Severinghaus *et al.* (*29*), Chapman *et al.* (*20*), and WOCE and CLIVAR data from section A22 in 1997 (*74*) and 2012 (*56*).

The TMI version 8 as described in Gebbie and Huybers (*32*) (www2.whoi.edu/staff/ggebbie/) was used to analyze deep water

composition in the GoM. A TMI advection diffusion matrix with 4° × 4° horizontal resolution (total of 2806 surface origin points) and 33 vertical levels was generated using inversion of six tracers: five from WOCE climatology [temperature, salinity, NO_3, PO_4, and O_2; (*75*)] and $\delta^{18}O$ data from global gridded oxygen isotopic composition dataset (*76*). The TMI matrix allows tracking the surface origin of the ocean interior. The position (90°W; 24°N) in the GoM at 3500-m depth was used to track the surface origin of these waters. As a result, the NA shows up as the major surface region contributing to deep GoM waters (fig. S3).

A set of CMIP6 GCMs (table S2) (*77*–*85*) was used to analyze 2000 to 2100 temperature and dissolved oxygen trends under the SSP585 and historical scenarios (*31*, *52*). The models have higher horizontal and vertical ocean resolution with finer resolution toward the surface and lower resolution toward the ocean interior. Some of the models have high enough resolution that allows mesoscale eddy permitting simulations [e.g., GFDL-CM4; (*79*)] with a realistic representation of GoM dynamics, resolving Loop Current System and anticyclonic eddies in the GoM. The models were also able to capture the general structure of the Yucatan transport with the main transport in the surface layer, representing the Loop Current, and some regions of deep outflow from the GoM. Temperature and oxygen output was averaged in the deep GoM below 2000 m. The temperature and oxygen trends show a strong increase and decrease, respectively, toward the end of the 21st century with very low internal variability in the deep GoM (Fig. 8).

Supplementary Materials

This PDF file includes:
Supplementary Text
Figs. S1 to S6
Tables S1 to S3
Legends for data S1 to S3

Other Supplementary Material for this manuscript includes the following:
Data S1 to S3

REFERENCES AND NOTES

1. W. J. Schmitz Jr., D. C. Biggs, A. Lugo-Fernández, L.-Y. Oey, W. Sturges, A synopsis of the circulation in the Gulf of Mexico and on its continental margins, in *Circulation in the Gulf of Mexico: Observations and Models, Alexis Lugo-Fernández and Wilton Sturges, Eds.* (American Geophysical Union, 2005), vol. 108, pp. 11–29.
2. P. Pérez-Brunius, H. Furey, A. Bower, P. Hamilton, J. Candela, P. García-Carrillo, R. Leben, Dominant circulation patterns of the deep gulf of Mexico. *J. Phys. Oceanogr.* **48**, 511–529 (2018).
3. P. Hamilton, R. Leben, A. Bower, H. Furey, P. Pérez-Brunius, Hydrography of the gulf of mexico using autonomous floats. *J. Phys. Oceanogr.* **48**, 773–794 (2018).
4. M. Tenreiro, J. Candela, E. Pallas-Sanz, J. Sheinbaum, J. Ochoa, Near-surface and deep circulation coupling in the western gulf of Mexico. *J. Phys. Oceanogr.* **48**, 145–161 (2018).
5. L.-Y. Oey, H.-C. Lee, Deep eddy energy and topographic Rossby waves in the Gulf of Mexico. *J. Phys. Oceanogr.* **32**, 3499–3527 (2002).
6. D. Rivas, A. Badan, J. Ochoa, The ventilation of the deep Gulf of Mexico. *J. Phys. Oceanogr.* **35**, 1763–1781 (2005).
7. E. Portela, M. Tenreiro, E. Pallàs-Sanz, T. Meunier, A. Ruiz-Angulo, R. Sosa-Gutiérrez, S. Cusí, Hydrography of the central and western Gulf of Mexico. *J. Geophys. Res. Oceans* **123**, 5134–5149 (2018).
8. W. J. Schmitz Jr., M. S. McCartney, On the North Atlantic circulation. *Rev. Geophys.* **31**, 29–49 (1993).
9. P. MacCready, W. E. Johns, C. G. Rooth, D. M. Fratantoni, R. A. Watlington, Overflow into the deep Caribbean: Effects of plume variability. *J. Geophys. Res.* **104**, 25913–25935 (1999).
10. I. Yashayaev, Hydrographic changes in the Labrador Sea, 1960–2005. *Prog. Oceanogr.* **73**, 242–276 (2007).
11. M. Rhein, D. Kieke, R. Steinfeldt, Advection of North Atlantic deep water from the Labrador Sea to the southern hemisphere. *J. Geophys. Res. Oceans* **120**, 2471–2487 (2015).
12. J. E. Hopkins, N. P. Holliday, D. Rayner, L. Houpert, I. Le Bras, F. Straneo, C. Wilson, S. Bacon, Transport variability of the irminger sea deep western boundary current from a mooring array. *J. Geophys. Res. Oceans* **124**, 3246–3278 (2019).
13. M. S. Lozier, F. Li, S. Bacon, F. Bahr, A. S. Bower, S. A. Cunningham, M. F. De Jong, L. De Steur, B. Deyoung, J. Fischer, S. F. Gary, B. J. W. Greenan, N. P. Holliday, A. Houk, L. Houpert, M. E. Inall, W. E. Johns, H. L. Johnson, C. Johnson, J. Karstensen, G. Koman, I. A. Le Bras, X. Lin, N. Mackay, D. P. Marshall, H. Mercier, M. Oltmanns, R. S. Pickart, A. L. Ramsey, D. Rayner, F. Straneo, V. Thierry, D. J. Torres, R. G. Williams, C. Wilson, J. Yang, I. Yashayaev, J. Zhao, A sea change in our view of overturning in the subpolar North Atlantic. *Science* **363**, 516–521 (2019).
14. W. Sturges, Deep exchange between the Atlantic, Caribbean, and Gulf of Mexico, in *Circulation in the Gulf of Mexico, Monograph 161, W. Sturges, A. Lugo-Fernandez, Eds.* (American Geophysical Union, 2005), pp. 263–278.
15. P. Hamilton, Topographic Rossby waves in the Gulf of Mexico. *Prog. Oceanogr.* **82**, 1–31 (2009).
16. S. Rahmstorf, J. E. Box, G. Feulner, M. E. Mann, A. Robinson, S. Rutherford, E. J. Schaffernicht, Exceptional twentieth-century slowdown in Atlantic Ocean overturning circulation. *Nat. Clim. Change* **5**, 475–480 (2015).
17. C. G. Piecuch, Likely weakening of the Florida Current during the past century revealed by sea-level observations. *Nat. Commun.* **11**, 3973 (2020).
18. W. Sturges, Water characteristics of the Caribbean Sea. *J. Mar. Res.* **23**, 147–161 (1965).
19. T. P. Buerkert, "Barium in water and foraminiferal shells: Indicator of oceanographic conditions in the Gulf of Mexico since the late Pleistocene," thesis, Louisiana State University, LA (1999).
20. P. Chapman, S. F. DiMarco, R. M. Key, C. Previti, S. Yvon-Lewis, Age constraints on Gulf of Mexico deep water ventilation as determined by14C measurements. *Radiocarbon* **60**, 75–90 (2018).
21. B. Dickson, I. Yashayaev, J. Meincke, B. Turrell, S. Dye, J. Holfort, Rapid freshening of the deep North Atlantic Ocean over the past four decades. *Nature* **416**, 832–837 (2002).
22. M. Rhein, R. Steinfeldt, D. Kieke, I. Stendardo, I. Yashayaev, Ventilation variability of Labrador SeaWater and its impact on oxygen and anthropogenic carbon: A review. *Phil. Trans. R. Soc. A.* **375**, 20160321 (2017).
23. L. Caesar, S. Rahmstorf, A. Robinson, G. Feulner, V. Saba, Observed fingerprint of a weakening Atlantic Ocean overturning circulation. *Nature* **556**, 191–196 (2018).
24. R. Dickson, J. Lazier, J. Meincke, P. Rhines, J. Swift, Long-term coordinated changes in the convective activity of the North Atlantic. *Prog. Oceanogr.* **38**, 241–295 (1996).
25. L. F Robinson, J. F. Adkins, L. D. Keigwin, J. Southon, D. P. Fernandez, S. L. Wang, D. S. Scheirer, Radiocarbon variability in the western north atlantic during the last deglaciation. *Science* **310**, 1469–1473 (2005).
26. J. Ochoa, V. Ferreira, J. Candela, J. Sheinbaum, M. López, P. Pérez-Brunius, S. Z. Herzka, R. M. W. Amon, Deep-water warming in the Gulf of Mexico from 2003 to 2019. *J. Phys. Oceanogr.* **51**, 1021–1035 (2021).
27. J. Candela, J. Ochoa, J. Sheinbaum, M. Lopez, P. Perez-Brunius, M. Tenreiro, E. Pallas-Sanz, G. Athie, L. Arriza-Oliveros, The flow through the Gulf of Mexico. *J. Phys. Oceanogr.* **49**, 1381–1401 (2019).
28. J. M. Morrison, W. J. Merrell Jr., R. M. Key, T. C. Key, Property distributions and deep chemical measurements within the western Gulf of Mexico. *J. Geophys. Res.* **88**, 2601–2608 (1983).
29. J. P. Severinghaus, W. S. Broecker, T. H. Peng, G. Bonani, Transect along 24°N latitude of ^{14}C in dissolved inorganic carbon in the subtropical North Atlantic Ocean. *Radiocarbon* **38**, 407–414 (1996).
30. V. Eyring, S. Bony, G. Meehl, C. A. Senior, B. Stevens, R. J. Stouffer, K. E. Taylor, Overview of the coupled model intercomparison project phase 6 (CMIP6) experimental design and organization. *Geosci. Model Dev.* **9**, 1937–1958 (2016).
31. B. C. O'Neill, E. Kriegler, K. Riahi, K. L. Ebi, S. Hallegatte, T. R. Carter, R. Mathur, D. P. van Vuuren, A new scenario framework for climate change research: The concept of shared socioeconomic pathways. *Clim. Change* **122**, 387–400 (2014).
32. G. Gebbie, P. Huybers, Total matrix intercomparison: A method for determining the geometry of water-mass pathways. *J. Phys. Oceanogr.* **40**, 1710–1728 (2010).
33. N. Gruber, J. Sarmiento, T. F. Stocker, An improved method for detecting anthropogenic CO_2 in the oceans. *Global Biogeochem. Cycles* **10**, 809–837 (1996).
34. R. M. Key, Ocean process tracers: Radiocarbon, in *Encyclopedia of Ocean Sciences, John H. Steele, Steve A. Thorpe, Karl K. Turekian, Eds.* (Academic Press 2001), pp. 2338–2353.
35. M. Stuiver, P. D. Quay, Atmospheric ^{14}C changes resulting from fossil fuel CO_2 release and cosmic ray flux variability. *Earth Planet. Sci. Lett.* **53**, 349–362 (1981).

36. S. I. Rubin, R. M. Key, Separating natural and bomb-produced radiocarbon in the ocean: The potential alkalinity method. *Global Biogeochem. Cycles* **16**, 52-1–52-19 (2002).
37. K. Lee, S.-D. Choi, G.-H. Park, R. Wanninkhof, T.-H. Peng, R. M. Key, C. L. Sabine, R. A. Feely, J. L. Bullister, F. J. Millero, A. Kozyr, An updated anthropogenic CO_2 inventory in the Atlantic Ocean. *Global Biogeochem. Cycles* **17**, 1116 (2003).
38. F. Touratier, L. Azouzi, C. Goyet, CFC-11, $\Delta^{14}C$ and ^3H tracers as a means to assess anthropogenic CO_2 concentrations in the ocean. *Tellus B. Chem. Phys. Meteorol.* **59**, 318–325 (2007).
39. E. R. M. Druffel, Decade time scale variability of ventilation in the North Atlantic: High-precision measurements of bomb radiocarbon in banded corals. *J. Geophys. Res.* **94**, 3271–3285 (1989).
40. W. S. Broecker, R. Gerard, Natural radiocarbon in the Mediterranean Sea. *Limnol. Oceanog.* **14**, 883–888 (1969).
41. P. P. Niiler, W. S. Richardson, Seasonal variability of the Florida Current. *J. Mar. Res.* **31**, 144–167 (1973).
42. E. van Sebille, M. O. Baringer, W. E. Johns, C. S. Meinen, L. M. Beal, M. F. de Jong, H. M. van Aken, Propagation pathways of classical Labrador Sea water from its source region to 26°N. *J. Geophys. Res.* **116**, C12027 (2011).
43. D. A. Smeed, S. A. Josey, C. Beaulieu, W. E. Johns, B. I. Moat, E. Frajka-Williams, D. Rayner, C. S. Meinen, M. O. Baringer, H. L. Bryden, G. D. McCarthy, The North Atlantic Ocean is in a state of reduced overturning. *Geophys. Res. Lett.* **45**, 1527–1533 (2018).
44. R. H. Smith, "Atlantic-Caribbean exchange through Windward Passage," thesis, University of Miami, FL (2010).
45. W. M. Smethie, R. A. Fine, A. Putzka, E. P. Jones, Tracing the flow of North Atlantic deep water using chlorofluorocarbons. *J. Geophys. Res.* **105**, 14297–14324 (2000).
46. A. S. Bower, M. S. Lozier, S. F. Gary, C. W. Boning, Interior pathways of the North Atlantic meridional overturning circulation. *Nature* **459**, 243–247 (2009).
47. T. P. Boyer, O. K. Baranova, C. Coleman, H. E. Garcia, A. Grodsky, R. A. Locarnini, A. V. Mishonov, C. R. Paver, J. R. Reagan, D. Seidov, I. V. Smolyar, K. Weathers, M. M. Zweng, World Ocean Database 2018. A.V. Mishonov, Technical Ed., NOAA Atlas NESDIS 87 (2018); www.ncei.noaa.gov/sites/default/files/2020-04/wod_intro_0.pdf.
48. W. Cheng, J. C. Chiang, D. Zhang, Atlantic meridional overturning circulation (AMOC) in CMIP5 models: RCP and historical simulations. *J. Climate* **26**, 7187–7197 (2013).
49. T. Hassan, R. J. Allen, W. Liu, C. A. Randles, Anthropogenic aerosol forcing of the Atlantic meridional overturning circulation and the associated mechanisms in CMIP6 models. *Atmos. Chem. Phys.* **21**, 5821–5846 (2021).
50. L. Kwiatkowski, O. Torres, L. Bopp, O. Aumont, M. Chamberlain, J. R. Christian, J. P. Dunne, M. Gehlen, T. Ilyina, J. G. John, A. Lenton, H. Li, N. S. Lovenduski, J. C. Orr, J. Palmieri, Y. Santana-Falcón, J. Schwinger, R. Séférian, C. A. Stock, A. Tagliabue, Y. Takano, J. Tjiputra, K. Toyama, H. Tsujino, M. Watanabe, A. Yamamoto, A. Yool, T. Ziehn, Twenty-first century ocean warming, acidification, deoxygenation, and upper-ocean nutrient and primary production decline from CMIP6 model projections. *Biogeosciences* **17**, 3439–3470 (2020).
51. A. Purich, M. H. England, Historical and future projected warming of Antarctic shelf bottom water in CMIP6 models. *Geophys. Res. Lett.* **48**, e2021GL092752 (2021).
52. M. J. Gidden, K. Riahi, S. J. Smith, S. Fujimori, G. Luderer, E. Kriegler, D. P. van Vuuren, M. van den Berg, L. Feng, D. Klein, K. Calvin, J. C. Doelman, S. Frank, O. Fricko, M. Harmsen, T. Hasegawa, P. Havlik, J. Hilaire, R. Hoesly, J. Horing, A. Popp, E. Stehfest, K. Takahashi, Global emissions pathways under different socioeconomic scenarios for use in CMIP6: A dataset of harmonized emissions trajectories through the end of the century. *Geosci. Model Dev.* **12**, 1443–1475 (2019).
53. A. H. Orsi, W. M. Smethie Jr., J. L. Bullister, On the total input of Antarctic waters to the deep ocean: A preliminary estimate from chlorofluorocarbon measurements. *J. Geophys. Res.* **107**, 31-1–31-14 (2002).
54. N. Tisnérat-Laborde, M. Paterne, B. Metivier, M. Arnold, P. Yiou, D. Blamart, S. Raynaud, Variability of the northeast Atlantic sea surface D14C and marine reservoir age and the North Atlantic Oscillation (NAO). *Quat. Sci. Rev.* **29**, 2633e2646 (2010).
55. A. Olsen, N. Lange, R. M. Key, T. Tanhua, M. Alvarez, S. Becker, H. C. Bittig, B. R. Carter, L. C. da Cunha, R. A. Feely, S. van Heuven, M. Hoppema, M. Ishii, E. Jeansson, S. D. Jones, S. Jutterström, M. K. Karlsen, A. Kozyr, S. K. Lauvset, C. Lo Monaco, A. Murata, F. F. Perez, B. Pfeil, C. Schirnick, R. Steinfeldt, T. Suzuki, M. Telszewski, B. Tilbrook, A. Velo, R. Wanninkhof, GLODAPv2.2019-an update of GLODAPv2. *Earth Syst. Sci. Data* **11**, 1437–1461 (2019).
56. R. Wanninkhof, R. A. Feely, F. J. Millero, R. Curry, D. A. Hansell, R. M. Key, J. Swift, W. M. Smethie, R. A. Fine, W. J. Jenkins, A. McNichol, E. R. M. Druffel, Dissolved inorganic carbon, pH, alkalinity, temperature, salinity and other variables collected from discrete sample and profile observations using Alkalinity titrator, CTD and other instruments from ATLANTIS in the Caribbean Sea and North Atlantic Ocean from 2012-03-24 to 2012-04-17 (NCEI Accession 0109915). NOAA National Centers for Environmental Information. Dataset (2013); https://doi.org/10.3334/cdiac/otg.clivar_a22_2012.
57. H. M. van Aken, M. F. de Jong, I. Yashayaev, Decadal and multidecadal variability of Labrador Sea Water in the north-western North Atlantic Ocean derived from tracer distributions: Heat budget, ventilation, and advection. *Deep Sea Res. I* **58**, 505–523 (2011).
58. D. G. Desbruyères, S. G. Purkey, E. L. McDonagh, G. C. Johnson, B. A. King, Deep and abyssal ocean warming from 35 years of repeat hydrography. *Geophys. Res. Lett.* **43**, 10356–10365 (2016).
59. S. Levitus, J. I. Antonov, T. P. Boyer, O. K. Baranova, H. E. Garcia, R. A. Locarnini, A. V. Mishonov, J. R. Reagan, D. Seidov, E. S. Yarosh, M. M. Zweng, World ocean heat content and thermosteric sea level change (0–2000 m), 2012. *Geophys. Res. Lett.* **39**, L10603 (2012).
60. M. J. Messias, H. Mercier, The redistribution of anthropogenic excess heat is a key driver of warming in the North Atlantic. *Commun. Earth Environ.* **3**, 118 (2022).
61. L. Chafik, N. P. Holliday, S. Bacon, T. Rossby, Irminger Sea is the center of action for subpolar AMOC variability. *Geophys. Res. Lett.* **49**, e2022GL099133 (2022).
62. L.-Y. Oey, T. Ezer, H.-C. Lee, Loop Current, rings and related circulation in the Gulf of Mexico: A review of numerical models and future challenges, in *Circulation in the Gulf of Mexico: Observations and Models*, W. Sturges, A. Lugo-Fernandez, Eds. (Geophysical Monograph Series, American Geophysical Union, 2005), vol. 161, pp. 31–56.
63. T. Tesi, F. Muschitiello, G. Mollenhauer, S. Miserocchi, L. Langone, C. Ceccarelli, G. Panieri, J. Chiggiato, A. Nogarotto, J. Hefter, G. Ingrosso, F. Giglio, P. Giordano, L. Capotondi, Rapid atlantification along the fram strait at the beginning of the 20th century. *Sci. Adv.* **7**, eabj2946 (2021).
64. D. J. R. Thornalley, D. W. Oppo, P. Ortega, J. I. Robson, C. M. Brierley, R. Davis, I. R. Hall, P. Moffa-Sanchez, N. L. Rose, P. T. Spooner, I. Yashayaev, L. D. Keigwin, Anomalously weak Labrador Sea convection and Atlantic overturning during the past 150 years. *Nature* **556**, 227–230 (2018).
65. L. Caesar, G. D. McCarthy, D. J. R. Thornalley, N. Cahill, S. Rahmstorf, Current atlantic meridional overturning circulation weakest in last millennium. *Nat. Geosci.* **14**, 118–120 (2021).
66. K. M. Johnson, J. M. Sieburth, P. J. L. Williams, L. Brandstrom, Coulometric total carbon dioxide analysis for marine studies: Automation and calibration. *Mar. Chem.* **21**, 117–133 (1987).
67. J. M. Hernández-Ayón, S. L. Belli, A. Zirino, pH, alkalinity and total CO_2 in coastal seawater by potentiometric titration with a difference derivative readout. *Anal. Chim. Acta* **394**, 101–108 (1999).
68. D. J. Hydes, M. Aoyama, A. Aminot, K. Bakker, S. Becker, S. Coverly, A. Daniel, A. Dickson, O. Grosso, R. Kerouel, J. Van Ooijen, K. Sato, T. Tanhua, M. Woodward, J. Zhang, Determination of dissolved nutrients (N, P, Si) in seawater with high precision and inter-comparability using gas-segmented continuous flow analysers, in The GO-SHIP Repeat Hydrography Manual: A Collection of Expert Reports and Guidelines, E. M. Hood, C. L. Sabine, B. M. Sloyan, Eds. (IOCCP Report 14, ICPO Publication Series 134, UNESCO-IOC, 2010); www.go-ship.org/HydroMan.html.
69. F. A. J. Armstrong, C. R. Stearns, J. D. H. Strickland, The measurement of upwelling and subsequent biological process by means of the Technicon Autoanalyzer® and associated equipment. *Deep-Sea Res. Oceanogr. Abstr.* **14**, 381–389 (1967).
70. M. Aoyama, D. J. Hydes, How do we improve the comparability of nutrient measurements? in *Comparability of Nutrients in the World's Ocean*, Aoyama, M.; Dickson, A.G.; Hydes, D.J.; Murata, A.; Oh, J.R.; Roose, P.; Woodward, E,M.S, Eds. (Mother Tank, 2010), pp. 1–10.
71. L. A. Anderson, J. L. Sarmiento, Redfield ratios of remineralization determined by nutrient data analysis. *Global Biogeochem. Cycles* **8**, 65–80 (1994).
72. W. S. Broecker, 'NO,' a conservative water-mass tracer. *Earth Planet. Sci. Lett.* **23**, 100–107 (1974).
73. B. Ribbat, W. Roether, K. O. Münnich, Turnover of eastern Caribbean deep water from 14C measurements. *Earth Planet. Sci. Lett.* **32**, 331–341 (1976).
74. K. M. Johnson, R. M. Key, F. J. Millero, C. L. Sabine, D. W. R. Wallace, C. D. Winn, L. Arlen, K. Erickson, K. Friis, M. Galanter, J. Goen, R. Rotter, C. Thomas, R. J. Wilke, T. Takahashi, S. C. Sutherland, Partial pressure (or fugacity) of carbon dioxide, dissolved inorganic carbon, pH, alkalinity, temperature, salinity and other variables collected from discrete sample and profile observations using CTD, bottle and other instruments from the KNORR in the Caribbean Sea and North Atlantic Ocean from 1996-11-02 to 1997-09-03 (NCEI Accession 0115005). NOAA National Centers for Environmental Information. (2013). Dataset (2019); https://doi.org/10.3334/cdiac/otg.ndp082.
75. V. Gouretski, K. P. Koltermann, WOCE global hydrographic climatology. *Berichte des BSH* **35**, 1–52 (2004).
76. A. N. LeGrande, G. A. Schmidt, Global gridded data set of the oxygen isotopic composition in seawater. *Geophys. Res. Lett.* **33**, L12604 (2006).
77. N. C. Swart, J. N. Cole, V. V. Kharin, M. Lazare, J. F. Scinocca, N. P. Gillett, J. Anstey, V. Arora, J. R. Christian, S. Hanna, Y. Jiao, W. G. Lee, F. Majaess, O. A. Saenko, C. Seiler, C. Seinen, A. Shao, M. Sigmond, L. Solheim, K. von Salzen, D. Yang, B. Winter, The Canadian earth system model version 5 (CanESM5. 0.3). *Geosci. Model Dev.* **12**, 4823–4873 (2019).

78. R. Séférian, C. Delire, B. Decharme, A. Voldoire, Y. M. D. Salas, M. Chevallier, D. Saint-Martin, O. Aumont, J.-C. Calvet, D. Carrer, H. Douville, L. Franchistéguy, E. Joetzjer, S. Sénési, Development and evaluation of CNRM Earth system model–CNRM-ESM1. *Geosci. Model Dev.* **9**, 1423–1453 (2016).
79. I. M. Held, H. Guo, A. Adcroft, J. P. Dunne, L. W. Horowitz, J. Krasting, E. Shevliakova, M. Winton, M. Zhao, M. Bushuk, A. T. Wittenberg, B. Wyman, B. Xiang, R. Zhang, W. Anderson, V. Balaji, L. Donner, K. Dunne, J. Durachta, P. P. G. Gauthier, P. Ginoux, J.-C. Golaz, S. M. Griffies, R. Hallberg, L. Harris, M. Harrison, W. Hurlin, J. John, P. Lin, S.-J. Lin, S. Malyshev, R. Menzel, P. C. D. Milly, Y. Ming, V. Naik, D. Paynter, F. Paulot, V. Ramaswamy, B. Reichl, T. Robinson, A. Rosati, C. Seman, L. G. Silvers, S. Underwood, N. Zadeh, Structure and performance of GFDL's CM4. 0 climate model. *J. Adv. Model. Earth Syst.* **11**, 3691–3727 (2019).
80. J. P. Dunne, L. W. Horowitz, A. J. Adcroft, P. Ginoux, I. M. Held, J. G. John, J. P. Krasting, S. Malyshev, V. Naik, F. Paulot, E. Shevliakova, C. A. Stock, N. Zadeh, V. Balaji, C. Blanton, K. A. Dunne, C. Dupuis, J. Durachta, R. Dussin, P. P. G. Gauthier, S. M. Griffies, H. Guo, R. W. Hallberg, M. Harrison, J. He, W. Hurlin, C. McHugh, R. Menzel, P. C. D. Milly, S. Nikonov, D. J. Paynter, J. Ploshay, A. Radhakrishnan, K. Rand, B. G. Reichl, T. Robinson, D. M. Schwarzkopf, L. T. Sentman, S. Underwood, H. Vahlenkamp, M. Winton, A. T. Wittenberg, B. Wyman, Y. Zeng, M. Zhao, The GFDL Earth system model version 4.1 (GFDL-ESM 4.1): Overall coupled model description and simulation characteristics. *J. Adv. Model. Earth Syst.* **12**, e2019MS002015 (2020).
81. O. Boucher, J. Servonnat, A. L. Albright, O. Aumont, Y. Balkanski, V. Bastrikov, S. Bekki, R. Bonnet, S. Bony, L. Bopp, P. Braconnot, P. Brockmann, P. Cadule, A. Caubel, F. Cheruy, F. Codron, A. Cozic, D. Cugnet, F. D'Andrea, P. Davini, C. de Lavergne, S. Denvil, J. Deshayes, M. Devilliers, A. Ducharne, J.-L. Dufresne, E. Dupont, C. Éthé, L. Fairhead, L. Falletti, S. Flavoni, M.-A. Foujols, S. Gardoll, G. Gastineau, J. Ghattas, J.-Y. Grandpeix, B. Guenet, L. E. Guez, E. Guilyardi, M. Guimberteau, D. Hauglustaine, F. Hourdin, A. Idelkadi, S. Joussaume, M. Kageyama, M. Khodri, G. Krinner, N. Lebas, G. Levavasseur, C. Lévy, L. Li, F. Lott, T. Lurton, S. Luyssaert, G. Madec, J.-B. Madeleine, F. Maignan, M. Marchand, O. Marti, L. Mellul, Y. Meurdesoif, J. Mignot, I. Musat, C. Ottlé, P. Peylin, Y. Planton, J. Polcher, C. Rio, N. Rochetin, C. Rousset, P. Sepulchre, A. Sima, D. Swingedouw, R. Thiéblemont, A. K. Traore, M. Vancoppenolle, J. Vial, J. Vialard, N. Viovy, N. Vuichard, Presentation and evaluation of the IPSL-CM6A-LR climate model. *J. Adv. Model. Earth Syst.* **12**, e2019MS002010 (2020).
82. T. Hajima, M. Watanabe, A. Yamamoto, H. Tatebe, M. A. Noguchi, M. Abe, R. Ohgaito, A. Ito, D. Yamazaki, H. Okajima, A. Ito, K. Takata, K. Ogochi, S. Watanabe, M. Kawamiya, Development of the MIROC-ES2L Earth system model and the evaluation of biogeochemical processes and feedbacks. *Geosci. Model Dev.* **13**, 2197–2244 (2020).
83. W. A. Müller, J. H. Jungclaus, T. Mauritsen, J. Baehr, M. Bittner, R. Budich, F. Bunzel, M. Esch, R. Ghosh, H. Haak, T. Ilyina, T. Kleine, L. Kornblueh, H. Li, K. Modali, D. Notz, H. Pohlmann, E. Roeckner, I. Stemmler, F. Tian, J. Marotzke, A higher-resolution version of the Max Planck Institute earth system model (MPI-ESM1. 2-HR). *J. Adv. Model. Earth Syst.* **10**, 1383–1413 (2018).
84. T. Mauritsen, J. Bader, T. Becker, J. Behrens, M. Bittner, R. Brokopf, V. Brovkin, M. Claussen, T. Crueger, M. Esch, I. Fast, S. Fiedler, D. Fläschner, V. Gayler, M. Giorgetta, D. S. Goll, H. Haak, S. Hagemann, C. Hedemann, C. Hohenegger, T. Ilyina, T. Jahns, D. Jimenéz-de-la-Cuesta, J. Jungclaus, T. Kleinen, S. Kloster, D. Kracher, S. Kinne, D. Kleberg, G. Lasslop, L. Kornblueh, J. Marotzke, D. Matei, K. Meraner, U. Mikolajewicz, K. Modali, B. Möbis, W. A. Müller, J. E. M. S. Nabel, C. C. W. Nam, D. Notz, S.-S. Nyawira, H. Paulsen, K. Peters, R. Pincus, H. Pohlmann, J. Pongratz, M. Popp, T. J. Raddatz, S. Rast, R. Redler, C. H. Reick, T. Rohrschneider, V. Schemann, H. Schmidt, R. Schnur, U. Schulzweida, K. D. Six, L. Stein, I. Stemmler, B. Stevens, J.-S. von Storch, F. Tian, A. Voigt, P. Vrese, K.-H. Wieners, S. Wilkenskjeld, A. Winkler, E. Roeckner, Developments in the MPI-M Earth system model version 1.2 (MPI-ESM1. 2) and its response to increasing CO_2. *J. Adv. Model. Earth Syst.* **11**, 998–1038 (2019).
85. S. Yukimoto, Y. Adachi, M. Hosaka, T. Sakami, H. Yoshimura, M. Hirabara, T. Y. Tanaka, E. Shindo, H. Tsujino, M. Deushi, R. Mizuta, S. Yabu, A. Obata, H. Nakano, T. Koshiro, T. Ose, A. Kitoh, A new global climate model of the meteorological research institute: MRI-CGCM3 —Model description and basic performance—. *J. Meteorol. Soc. Japan. Ser. II* **90**, 23–64 (2012).
86. W. Sturges, Observations of deep-water renewal in the Caribbean Sea. *J. Geophys. Res.* **75**, 7602–7610 (1970).
87. W. J. Jenkins, Oxygen utilization rates in North Atlantic subtropical gyre and primary production in oligotrophic systems. *Nature* **300**, 246–248 (1982).

Acknowledgments: We thank the captain, scientists, and crew of the *R/V Pelican* and *B/O Justo Sierra* for help during the cruises. Special thanks go to V. Ferreira for discussions during the cruises and during a faculty development leave at CICESE (R.M.W.A.). The processing of raw CTD data has been carried out by J. Garcia. We also want to acknowledge the team at the UCI Keck Carbon Cycle AMS Laboratory (X. Xu and J. Walker) for help and high-quality radiocarbon data and B. Walker and A. Orsi for discussions and advice. **Funding:** This work was supported by the Mexican National Council for Science and Technology–Mexican Ministry of Energy–Hydrocarbon Fund, project 201441. Mooring data were generated with CICESE overhead funds. This is a contribution of the Gulf of Mexico Research Consortium (CIGoM). We acknowledge PEMEX's specific request to the Hydrocarbon Fund to address the environmental effects of oil spills in the GoM. During the course of this work, we suffered the tremendous loss of two of our coauthors, J.O. (May 2020) and J.C. (November 2022). They were wonderful human beings and outstanding scientists who contributed ideas and work that made this study possible. Their friendship, leadership, and wit will always be remembered. We wish to dedicate this article in their memory. **Author contributions:** Conceptualization: R.M.W.A., J.O., S.Z.H., J.C.H., J.S., and J.C. Methodology: R.M.W.A., J.O., J.C., S.M., S.Z.H., P.P.-B., V.F.C.I., M.H.A., R.M.K., and J.C.H. Investigation: R.M.W.A., J.O., J.C., S.Z.H., P.P.-B., J.C.H., V.F.C.I., and M.H.A. Visualization: R.M.W.A., J.O., J.C., and S.M. Supervision: R.M.W.A., J.C., and S.Z.H. Writing—original draft: R.M.W.A. Writing—review and editing: R.M.W.A., R.M.K., J.O., J.C., S.Z.H., P.P.-B., J.S.P., V.F.C.I., M.H.A., J.C.H., and S.M. **Competing interests:** The authors declare that they have no competing interests. **Data and materials availability:** Hydrographic data including radiocarbon, alkalinity, nutrients, and dissolved oxygen used to calculate the radiocarbon-based residence times are summarized in table S3 in the Supplementary Materials, and data sources from other cruises are indicated in the reference list. All other high-resolution CTD data (hydrographic_data), data used for the deep volume transport calculations (physical_data_restimes.mat), the code for calculating volume transport–based residence times (compute_restimes.m), and an explanation for the volume transport data (README_FIG 5.txt) needed to evaluate the conclusions in the paper are present as separate files in the Supplementary Materials. The codes used for the TMI were downloaded from www2.whoi.edu/staff/ggebbie/ using the following link: https://drive.google.com/drive/folders/1nFDSINbst84pK68aWwRGBVfYZkfN1mUR. To process CMIP6 data, we used Python codes available at https://doi.org/10.5281/zenodo.7596504 together with computational resources provided by Pangeo Cloud processing services (https://pangeo.io/). All the CMIP6 model output under historical and future projections can be downloaded from the Earth System Grid Federation (ESGF) at https://esgf-data.dkrz.de/search/cmip6-dkrz/. All data needed to evaluate the conclusions in the paper are present in the paper and/or the Supplementary Materials.

Submitted 28 July 2022
Accepted 10 February 2023
Published 17 March 2023
10.1126/sciadv.ade1685